The influence of aerosol hygroscopicity on precipitation intensity during a mesoscale convective event

1. Stacey Kawecki, Department of Climate and Space Sciences and Engineering, University of Michigan, Ann Arbor, MI 48109

2. Allison L. Steiner, Department of Climate and Space Sciences and Engineering, University of Michigan, Ann Arbor, MI 48109

Corresponding Author: Stacey Kawecki, slekaw@umich.edu, 2455 Hayward St, Ann Arbor, MI 48109

Key Points

1. Aerosol composition can affect spatial patterns of precipitation.
2. Hygroscopicity and hydrometeor vertical distributions are sensitive to aerosol composition and impact precipitation processes.
3. Altering speciated aerosol hygroscopicity can influence the simulation of precipitation intensity.

This is the author manuscript accepted for publication and has undergone full peer review but has not been through the copyediting, typesetting, pagination and proofreading process, which may lead to differences between this version and the Version of Record. Please cite this article as doi: 10.1002/2017JD026535

Abstract

We examine how aerosol composition affects precipitation intensity using the Weather and Research Forecasting Model with Chemistry (version 3.6). By changing the prescribed default hygroscopicity values to updated values from laboratory studies, we test model assumptions about individual component hygroscopicity values of ammonium, sulfate, nitrate, and organic species. We compare a baseline simulation (BASE, using default hygroscopicity values) with four sensitivity simulations (SULF, increasing the sulfate hygroscopicity; ORG, decreasing organic hygroscopicity; SWITCH, using a concentration-dependent hygroscopicity value for ammonium; and ALL, including all three changes) to understand the role of aerosol composition on precipitation during a mesoscale convective system (MCS). Overall, the hygroscopicity changes influence the spatial patterns of precipitation as well as the intensity. Focusing on the maximum precipitation in the model domain downwind of an urban area, we find that changing the individual component hygroscopicities leads to bulk hygroscopicity changes, especially in the ORG simulation. Reducing bulk hygroscopicity (e.g., ORG simulation) initially causes fewer activated drops, weakened updrafts in the mid troposphere, and increased precipitation from larger hydrometeors. Increasing bulk hygroscopicity (e.g., SULF simulation) simulates more numerous and smaller cloud drops and increases precipitation. In the ALL simulation, a stronger cold pool and downdrafts lead to precipitation suppression later in the MCS evolution. In this downwind region, the combined changes in hygroscopicity (ALL) reduces the over-prediction of intense events (>70 mm d^{-1}) and better captures the range of moderate intensity (30-60 mm d^{-1}) events.

The results of this single MCS analysis suggest that aerosol composition can play an important role in simulating high-intensity precipitation events.

Introduction

Atmospheric aerosols can affect clouds, weather and climate, yet their influence on cloud processes at varying spatial and temporal scales is highly uncertain (Stevens and Feingold 2009; Boucher et al. 2013; Fan et al. 2016). From the climate perspective, aerosols can alter the optical properties of the cloud (known as the first indirect effect; (Twomey 1977)) or change precipitation processes (known as the second indirect effect; (Albrecht 1989)). On shorter timescales, such as those governing deep convective clouds and severe weather, studies suggest that aerosols can affect weather events (Andreae et al. 2004; Tao et al. 2012; Saide et al. 2015). Within the meteorology community, it is widely accepted that cloud condensation nuclei (CCN) number and size distribution are dominant in determining aerosol indirect effects (Khain et al. 2000; Dusek et al. 2006). However, the chemical composition of aerosols also influences its ability to act as CCN (Ekman et al. 2004; Fan et al. 2007). Specifically, some aerosol components are known to be extremely effective CCN (e.g., ammonium sulfate; (Easter and Hobbs 1974)), ice nuclei (IN; e.g., mineral dust; (DeMott et al. 2003)) or light absorbers (elemental carbon, soot, (Andreae and Gelencsér 2006)). While aerosol composition is studied in detail within the atmospheric chemistry community, composition effects are not traditionally included in meteorology models because of limited computing capabilities and the prioritization of efficiently representing microphysical processes (Ghan and Schwartz 2007; Khain et al. 2015). In many studies, CCN fields are prescribed using a fixed

chemical composition of ammonium sulfate (Van den Heever et al. 2006; Carrió et al. 2010; Eidhammer et al. 2014). In this manuscript, we examine the sensitivity of the simulation of a severe weather event to the representation of chemical composition of aerosols, with the goal of testing the mechanistic understanding of the role of aerosol composition on mesoscale convective weather systems (Marinescu et al. 2016; Saleeby et al. 2016).

Because of the favorable synoptic conditions, the United States Central Great Plains (CGP) frequently experiences convective weather in the form of mesocscale convective systems (MCSs). MCSs are defined as a complex of thunderstorms that organize on a scale larger than individual thunderstorms, persist for several hours or more, and develop a mesoscale circulation. MCSs have precipitation resulting from both convective and stratiform clouds and contribute to the formation of cirrus anvil clouds, making them radiatively relevant (Houze 2004; Fan et al. 2012). Additionally, MCSs are important because they produce intense precipitation that can damage crops and property as well as cause human injuries and fatalities. For example, from 1980 to 2011, severe local storms in the United States contributed to 94.6 billion dollars in damage (Smith and Katz 2013). Therefore it is imperative to understand the atmospheric processes that drive these systems. Within these thunderstorms, unstable air rises and cloud drops form as the parcel of air reaches the lifted condensation level (LCL), releasing latent heat. This release of latent heat contributes to the instability of the air parcel, increasing the parcel's buoyancy and leading to stronger updraft velocities. Stronger updraft velocities enable greater vertical development, often reaching temperatures well below freezing, while the process of collision and coalescence aids in the formation of raindrops. Solid

hydrometeors form during this transition into the mid and upper levels of the troposphere, including graupel (and/or hail), snow, and ice crystals (Dudhia 1996).

Aerosols play a complex role in deep convective clouds that constitute MCSs (Fan et al. 2016) because water may exist in all three phases, requiring an understanding of both warm and cold clouds. In warm, shallow, and precipitating clouds, increasing the number of hygroscopic aerosols increases the number of available cloud condensation nuclei (CCN), leading to smaller droplets and reduced precipitation rates (Rosenfeld 2000; Rosenfeld et al. 2008; Fan et al. 2013; Rosenfeld et al. 2014; Saleeby et al. 2015). These smaller droplets have been hypothesized to invigorate convection within deep convective systems as they can be lofted to higher altitudes, cause more mass to freeze, and release latent heat that further feeds the updraft (Van den Heever et al. 2006; van den Heever and Cotton 2007; Lebo and Seinfeld 2011, Sheffield et al, 2015). Further, changes in aerosol concentrations have been shown to affect the macrophysical properties of cloud systems and the subsequent precipitation patterns (Ntelekos et al. 2009; Cerully et al. 2015; Kawecki et al. 2016). In cold clouds, aerosols affect ice nucleation rates through heterogeneous freezing processes (e.g., immersion freezing, contact freezing). In mixed phase clouds, the interaction between warm and cold phases are important as ice crystals (snow) can grow at the expense of liquid water (cloud drops) via the Wegener-Bergeron-Findeisen (WBF) process and riming, and influence cloud microphysical processes (Storelvmo and Tan 2015).

In warm clouds, aerosol activation as CCN is the first step in cloud and precipitation processes and is determined by several factors: the environmental supersaturation, the size of the aerosol, and the aerosol's composition (Köhler 1936).

Aerosol hygroscopicity, a metric that describes the rate of water vapor uptake by an aerosol, can be measured in the laboratory and is determined by chemical speciation and dry diameter size. Petters and Kreidenweis (2007) developed the "kappa" parameterization that uses aerosol hygroscopicity, dry diameter and the environmental supersaturation to determine whether or not aerosols will activate. This type of parameterization has been implemented into meteorology-chemistry models such as the Regional Atmospheric Modeling System (RAMS; (Pielke et al. 1992), (Cotton et al., 2003)) and Weather and Research Forecasting Model with Chemistry (WRF-Chem; (Grell et al. 2005)). Because WRF-Chem has been shown to accurately simulate meteorological and chemical processes of aerosols, Ward and Cotton (2011) used WRF-Chem simulations to provide cloud droplet number concentration and speciated aerosol information to RAMS simulations. Using the kappa parameterization, they evaluated differences between the hygroscopicity in the default WRF-Chem and those from lab-derived studies and found that organic hygroscopicities were overestimated and most inorganic species were underestimated with the default WRF-Chem parameterization. While this work evaluated the changes in hygroscopicity with the use of model-specified defaults, they did not evaluate the impact of these changes on meteorological processes and if these processes are sensitive to the spatial heterogeneity of aerosol mass and composition.

Several studies have investigated how aerosol composition can affect short-term weather on several severity scales. Many of these studies have focused on light absorbing carbon from biomass burning events, as emissions are large in magnitude and these aerosols have strong direct (Ackerman et al. 2000), indirect (Wang et al. 2009) and

semi-direct effects (Fan et al. 2015). For example, Zhang et al. (2016) found that the presence of biomass burning aerosols can influence the accuracy of numerical weather prediction, where observed 2-meter temperatures are lower than simulated due to reduced surface radiation and altered boundary layer stability. Saide et al. (2015) showed that smoke from biomass burning in Central America increases the probability of tornadoes in the US Central Great Plains by lowering the LCL and affecting low-level wind shear. Other studies of light-absorbing aerosols from anthropogenic sources have been found to modify and even cause extreme precipitation events (Fan et al. 2015).

Here, we explore the role of aerosol hygroscopicity on severe weather events and expand this evaluation beyond light absorbing aerosols. We simulate a mesoscale convective system in the Central United States using the WRF-Chem to determine the sensitivity of precipitation intensity and spatial patterns to aerosol composition. Section 2 describes methods, model parameterizations, and the experimental setup to investigate the role of aerosol hygroscopicity through a series of sensitivity tests that alter the model-prescribed kappa values for sulfate, nitrate, and organic species. In section 3, we discuss the results and Section 4 follows with discussion and conclusions. These sensitivity tests show that accumulated precipitation patterns and the duration and intensity of precipitation are sensitive to the representation of aerosol hygroscopicity within the WRF-Chem model.

2.0 Methods

2.1 WRF-Chem description

To examine the effects of aerosol hygroscopicity on precipitation intensity during a severe weather event, we use the WRF Model with online chemistry (WRF-Chem v 3.6; Grell, 2005). We simulate a mesoscale convective system that occurred on May 27, 2013 near Kansas City, MO, described in detail in Kawecki et al. (2016). This system produced large amounts of rain and severe weather, including hail with diameters equal to or exceeding 1 inch (2.54 cm) and wind gusts exceeding 58 miles per hour (26 m s^{-1}). The model domain is centered on Kansas City, Missouri, a mid-sized city surrounded by agriculture (Figure 1). This region allows us to examine interactions of several types of aerosols, including organic aerosols derived from anthropogenic volatile organic compound (VOC) emissions, ammonium nitrate and ammonium sulfate formed as a result of agricultural ammonia emissions interacting with the nitrates and sulfates from urban areas and power generation.

The model is configured with a horizontal grid cell resolution of 4 km and 72 vertical levels. While the 4-km horizontal grid size does not likely explicitly resolve this type of system, this squall line is driven by synoptic scale meteorology that has been successfully simulated in previous work (Kawecki et al., 2016). Meteorological boundary conditions are from the NAM-Reanalysis (12 km; (NCEI 2013)) and chemical boundary conditions are provided from MOZART-GEOS4 simulations (Emmons et al. 2010) and updated every 6 hours. We use the Morrison microphysics parameterization (Morrison et al. 2005), which is a two-moment scheme that tracks five hydrometeor species (cloud drop, raindrop, graupel, snow, ice and water vapor). Radiation is parameterized with the RRTMG for both long-wave and shortwave radiation schemes (Price et al. 2014). Boundary layer processes are parameterized using the Yonsei University scheme (Hong

et al. 2006), surface layer parameters are resolved using the Monin-Obukhov scheme and the land surface is parameterized with the Noah land surface model (Ek et al. 2003) with the urban canopy model implementation. For chemistry, we use the RADM2 gas phase chemical mechanism (Stockwell et al. 1990) and MADE-SORGAM (Schell et al. 2001) aerosol model. Anthropogenic emissions are from the 2013 United States Environmental Protection Agency (EPA) National Emissions Inventory (NEI; EPA 2011) gridded to the 4km model resolution. Biogenic isoprene emissions follow the MEGAN model (version 2; (Guenther et al. 2006)). Photolysis rates and reactions are calculated using the Fast-J photolysis scheme (Wild et al. 2000). Additional details on the meteorological event evaluation are described in Kawecki et al. (2016).

2.2 MADE/SORGAM Aerosol Parameterization

Aerosol size distributions are described by three internally mixed, lognormal modes (Aitken, accumulation and coarse) in the MADE/SORGAM aerosol mechanism (Schell et al. 2001). The Aitken and accumulation modes each have 16 chemical species, including primary un-speciated $PM_{2.5}$ ("p25"), sulfate, ammonium, nitrate, sodium, chlorine, elemental carbon, primary organic aerosol ("orgpa"), and eight categories of secondary organic aerosol (SOA). SOA categories include one from alkanes ("orgalk1"), one from olefins ("orgole1"), two formed from aromatics ("orgaro1" and "orgaro2"), and four from biogenic VOC ("orgba1", "orgba2", "orgba3", "orgba4"). The coarse mode comprises sea salt, soil-derived aerosol, and unspecified primary anthropogenic emissions, characterized as internally mixed continental aerosol.

There are three mechanisms for aerosols to enter one of the aerosol modes: primary emission, secondary formation, and new particle formation from sulfuric acid nucleation based on Kulmala et al. (1998). Primary emissions include dust, anthropogenic emissions of inorganic and organic $PM_{2.5}$ in the Aitken and accumulation modes, sea salt and biomass burning. We note that in the simulations presented here, we do not include interactive dust (although some anthropogenic dust is emitted from urban areas in the US NEI), sea salt, or biomass burning emissions. Secondary formation of organic aerosol is simulated by the SORGAM mechanism, which allows condensation of organic mass based on estimated product yields (Schell et al. 2001).

The internally mixed aerosol modes are tracked as either clear air particles (interstitial) or cloud-borne (in-cloud) particles. Interstitial aerosols are activated as cloud drops based on the maximum supersaturation determined from a Gaussian spectrum of updraft velocities and internally mixed aerosol properties (i.e. hygroscopicity and density) within each mode (Chapman et al. 2009). These activated aerosols are then traced as "in-cloud" aerosol. Aerosols in each mode can also become in-cloud aerosol via precipitation scavenging, and the in-cloud aerosol can return to interstitial aerosols when cloud drops and raindrops evaporate. Currently, the MADE/SORGAM parameterization as implemented in WRF-Chem does not explicitly include the activation of aerosols as ice nuclei, as the ice nucleation rate is represented as a function of temperature and ice supersaturation only.

2.3 Hygroscopicity and implementation of the kappa parameterization

In the model configuration used in this study, each aerosol type is assigned a default hygroscopicity value by WRF-Chem (Table 1). For every grid cell at each time step, the volume-weighted bulk hygroscopicity is calculated for each of the three modes for interstitial aerosol. These bulk hygroscopicities are then used to activate a portion of the aerosols as CCN (or in-cloud aerosol) depending on the environmental supersaturation (Abdul - Razzak and Ghan 2000). Because the aerosol modes are internally mixed, it is important to understand the hygroscopicities of all chemical species. Within the model domain sub-region downwind of Kansas City (Figure 1a), the most abundant aerosols are sulfate, ammonium, and nitrate (Figure 1), which are all assigned the same hygroscopicity value (0.5) in the default WRF-Chem (Table 1). Organic species have a relatively low hygroscopicity (default of 0.14; Table 1), and elemental carbon is prescribed an extremely low value (1.0×10^{-6}).

Because of the dominance of inorganic species in the region, the interactions between sulfate, nitrate and ammonium are key to determining the overall composition and hygroscopicity of aerosol. Ammonia is an important neutralizing gas in the atmosphere (Behera et al. 2013), and tends to react quickly with either sulfuric or nitric acid in the atmosphere to form aerosols. Generally the formation of ammonium sulfate is favored, and due to its low vapor pressure, this process is essentially irreversible:

(R1) $NH_3 + H_2SO_4 \rightarrow NH_4HSO_{4s,aq}$

(R2) $2NH_3 + H_2SO_4 \rightarrow (NH_4)_2SO_{4s,aq}$

However, the ratio of ammonium to sulfate is important for determining whether ammonium will form either ammonium sulfate or ammonium nitrate. Values greater

than two encourage reaction with nitrates (Ackermann et al. 1998), where ammonium nitrate can be formed via a reversible reaction:

(R3) $NH_3 + HNO_3 <--> NH_4NO_3$

Laboratory studies show that the hygroscopicity of ammonium depends on whether it is partitioned with sulfate or nitrate (Petters and Kreidenweis 2007). However, WRF-Chem default hygroscopicity values are all the same for these three components (Table 1).

Organic aerosol formed by the oxidation of aromatics have lab-derived hygroscopicity values of 0.051 and 0.094 respectively (Petters and Kreidenweis 2007), while aerosol derived from alkanes has a hygroscopicity value of 0.005 (Virkkula et al. 1999; Raymond and Pandis 2002; VanReken et al. 2005; Petters et al. 2009), a full order of magnitude lower than the default. Olefin-derived organic aerosol has been observed to have the highest organic hygroscopicity at 0.19 (Petters and Kreidenweis 2007). The current default settings in WRF-Chem include organics as one category of "organic carbon" with a single hygroscopicity that is applied to all SOA of 0.14, which is not representative of these laboratory values (Ward and Cotton 2011).

The default hygroscopicities representing individual components in the standard version of WRF-Chem have not been explored or tested extensively. As shown above, several of the organics are misrepresented in the model with higher hygroscopicity than observed, while the default hygroscopicity of ammonium sulfate and nitrate are lower than observed and do not account for the partitioning of ammonium. The internal mixtures of the three aerosol modes depend on the spatial heterogeneity of the aerosols and their chemical process, and this internal mixture in turn determines the bulk hygroscopicity and the activating potential of the aerosols. Because the first step in cloud

formation is the droplet activation, it is important to test the hygroscopicity assumptions that drive activation and subsequent precipitation processes through sensitivity simulations.

2.4 Experimental Design

To test the simulated precipitation duration and intensity sensitivity to aerosol hygroscopicity, we run five 60-hour simulations of a severe weather event on May 27, 2013 near Kansas City, MO. In the first simulation, we use the default hygroscopicity values provided in WRF-Chem (Table 1), hereinafter called the "BASE" case. We then conduct several sensitivity tests to examine the role of individual species' hygroscopicity by systematically changing hygroscopicity values in the MADE/SORGAM data module in WRF-Chem based on the suggested values in Ward and Cotton (2011) (Table 1). In the second simulation (SULF), we increase the sulfate hygroscopicity value from 0.5 to 0.71 (Petters and Kreidenweis 2007). For the third simulation (ORG), we change the values of the SOA formed from anthropogenic precursor VOC to laboratory-tested values (Table 1 for orgalk1, orgaro1, orgaro2, orgole1, orgpa) (Virkkula et al. 1999; VanReken et al. 2005; Petters et al. 2009), which overall reflects a decrease in the hygroscopicity of organic aerosol species. For the fourth simulation (SWITCH), we incorporate a "switch" for ammonium. If the ratio of ammonium to sulfate is greater than 2.0, ammonia reacts with nitrates to form ammonium nitrate, leading to an ammonium hygroscopicity of 0.67. If the ratio is less than two, the formation of ammonium sulfate is likely, resulting in a lower hygroscopicity of 0.5. Finally, we conduct a fifth simulation to provide an up-to-date representation of aerosol hygroscopicity from recent laboratory studies and

incorporate all of the changes to the hygroscopicity values from Table 1 (ALL). The comparison of these simulations and their effects on a severe weather event is described in Section 3.0 below.

2.5 Aerosol Simulation Evaluation

The Central Great Plains simulation domain provides a unique blend of agriculture and industrial emissions (Kawecki et al. 2016). In the continental United States, ammonia emissions are increasing (Butler et al. 2016), while industrial emissions are declining (Hand et al. 2012). Additionally, sulfur dioxide (SO_2) emissions have substantially decreased since 2002 (Hand et al. 2012), reducing concentrations of sulfur dioxide (SO_2) and sulfuric acid (H_2SO_4) across the US. Prior model evaluation suggested that the sulfate concentrations at the model boundaries as provided by the MOZART chemical boundary conditions simulated too much sulfate as compared to ground-based observations (Kawecki et al. 2016), and here we remove incoming sulfate and sulfuric acid at all boundaries to improve our evaluation of simulated sulfate with ground-based observations from IMPROVE (Malm et al. 1994) observational network (Figure 1). We note that the IMPROVE site data is the average of May 22 and May 25 2013 samples, while the model data is the boundary layer average of a 3x3 grid cell average 144 km^2 region containing the location of the site from May 26 06:00 UTC to May 27 06:00 UTC,

Despite the elimination of model boundary sulfur compounds, the model still shows a slight bias for ammonium sulfate and ammonium nitrate at the two IMPROVE locations within the model domain (El Dorado Springs, MO; and Lake Seguma, IA; Figure 1). At the Lake Seguma site, the modeled ammonium sulfate (2.15 μg m^{-3}) and

ammonium nitrate (2.11 μg m^{-3}) are about 1.75 times and 2.85 times greater than observed, which are 1.24 μg $m^{-3}$and 0.74 μg m^{-3} respectively. The observed and modeled organic carbon is similar, with the model slightly lower than the observed value of 0.67 μg m^{-3}. Even though there are discrepancies between the observed and modeled aerosol constituents, the model replicates the balance between ammonium, nitrate, sulfate and organics in this region. Elemental carbon is lower than observed, likely because biomass burning emissions are not included.

$PM_{2.5}$ is clearly associated with urban regions (Figure 1a), with plume concentrations of 5.5 μg m^{-3} originating from Oklahoma City and Tulsa in the southwestern portion of the domain, and a plume of $PM_{2.5}$ (5.5 μg m^{-3}) extending northward from Kansas City in the center of the domain. In comparison with the IMPROVE sites in the eastern portion of the domain, the model represents the speciated $PM_{2.5}$ fairly well at both locations. At the EDS site southeast of Kansas City, the model simulates similar amounts of ammonium sulfate and organic carbon, with slightly more simulated than observed for ammonium nitrate (0.51 μg m^{-3} simulated versus 0.29 μg m^{-3} observed). The model underrepresents elemental carbon, where the observed is about 0.35 μg m^{-3}, approximately 2.5 times that simulated by the model which may be due to the lack of biomass burning emissions in the model. Though ammonium sulfate and nitrate is over-predicted in the northern portion of the simulations, the rain event that we focus on is to the west and south of this model bias, and will not likely affect the simulation of bulk aerosol hygroscopicity. The chemical composition of the aerosols east of Kansas City (Figure 1d) is well balanced between ammonium nitrate, ammonium sulfate and organics. Nitrates and sulfates dominate the mixture with averages of 1.7μg

m^{-3} and 1.65, respectively, while the organics make up most of the remaining fraction ($1.0\ \mu g\ m^{-3}$). Generally, the model evaluates well against the limited composition measurements available within the model domain.

3.0 Results

We evaluate the changes in precipitation patterns and intensity as simulated by WRF-Chem due to alterations of aerosol hygroscopicity values. We examine how changing the individual hygroscopicity values alters precipitation patterns and intensity (Section 3.1). Next, we evaluate the effect of altering species' hygroscopicities on the accumulation mode and assess how these changes in hygroscopicity affect the hydrometeor number concentrations and sizes (Section 3.2). To link the aerosol changes to dynamics, we discuss the changes to the cold pools and precipitation as a function of hygroscopicity changes (Section 3.3). Finally, we compare model results to observations of daily-accumulated precipitation from May 27, 2013 (Daymet and NCEP Stage IV; (Thornton et al. 2016, Lin 2011)) to assess the realism of these sensitivity tests (Section 3.4)

3.1 Meteorological Description and Precipitation Intensity Frequency

An intense rainfall event occurred near Kansas City, MO on May 27, 2013 (Figure 2) as a mesoscale convective system crossed the region, spawning severe weather with large hail and strong winds. The regions of most intense precipitation as per the observed data (NCEP Stage IV precipitation (Lin 2011)) occur west and northwest of Kansas City, in Kansas and Nebraska (Figure 2a). A second region of widespread

accumulation occurs to the east and north of Kansas City. Both regions have accumulations exceeding 100 mm over relatively small areas. Previous work has shown the model represents this event by approximating the placement and timing of the storm cells (Kawecki et al. 2016). Figure 2b shows the accumulated precipitation for the BASE simulation over the 24 hour period, reaching up to 100 mm in the region to the south of the city and extending eastward along the storm track. The four sensitivity simulations with altered hygroscopicity (Figures 2c-f) have a pattern similar to the BASE simulation with a swath of precipitation starting at the junction of the Platt and Missouri Rivers and continuing southeast. While the domain-averaged accumulated precipitation does not change substantially with changing hygroscopicity, the spatial distribution of heavy precipitation does. For example, in the SULF simulation, the maximum precipitation occurs to the east of Kansas City (Figure 2c), with high values (> 100 mm) covering a greater spatial extent than the BASE simulation. In the ORG simulation that reduced the hygroscopicity of organic aerosols, the Kansas City local precipitation maximum is contiguous to regions of higher precipitation to the east (Figure 2d) with precipitation amounts exceeding 100 mm. The SWITCH simulation, which allows different hygroscopicity values of ammonium depending on the partitioning, shows the greatest change from the BASE simulation with greater precipitation accumulation (Figure 2e). The region with values exceeding 100 mm is to the north and east of Kansas City and is larger and more contiguous than in the other simulations. Finally, the ALL (Figure 2f) simulation, which incorporates all updated hygroscopicity changes, also resembles the BASE simulation with respect to both precipitation amounts and spatial patterns.

Rainfall intensity is a measure of the amount of rain (mm) that falls over a given amount of time (hour). While rainfall intensity does not determine whether a storm is classified as a severe threat or not, flooding and flash flooding are imminent dangers associated with high-intensity rainfall events. According to the American Meteorological Society (AMS), heavy rain accrues at a rate of more than 8 mm $hour^{-1}$. To examine how often heavy or high-intensity rainfall (HIR) occurs, we count the number of times each grid cell has greater than 10 mm $hour^{-1}$ during the final 24 hours of the simulations (Figure 2g-k). In the BASE simulation, there are two main regions where HIR occurs: (1) in the northwestern quadrant of the domain (40.5 - 41.0°N and 95.0-97.0°W), and (2) in the eastern portion of the domain around 39.5°N extending from Kansas City to the east. Like the accumulated precipitation, all four sensitivity simulations show a similar spatial pattern of HIR occurring along the storm track that moved from the northwest corner of the domain to the southeast. Generally, the largest HIR values occur concurrently with the largest values of accumulated precipitation. In the BASE case, there are only a few grid cells that have HIR exceeding 4 hours (Figure 2g). The SULF HIR overall pattern matches the BASE case, with more grid cells simulating higher HIR values especially on the southeastern edge of the system (Figure 2h). In the ORG simulation (Figure 2i), the southeastern portion of the rain event looks similar to the SULF simulation with reduced HIR. When including the switch for ammonium nitrate, the region east of Kansas City has maxima exceeding 8 hours of HIR (Figure 2j), which coincides with the large amounts of accumulated precipitation in this region (Figure 2d). Similar to precipitation accumulation, the ALL simulation HIR is similar to the BASE simulation, with the same pattern and magnitude of HIR (Figure 2k).

When averaged over the entire domain, the differences in precipitation occurring between the simulations are small (not shown). However, when examined spatially, the differences can be substantial. For example, there is a large increase in accumulated precipitation east of Kansas City in the SWITCH simulation. The spatial discrepancies and intensity changes of precipitation associated with altering aerosol hygroscopicity suggest that mesoscale circulations are most likely being impacted by the aerosol property changes. To focus on aerosol-driven impacts on the event, we analyze the time period during the most intense area of the storm near Kansas City, MO [0000 – 1800 UTC 5-27-2013]. Spatially, the region east of Kansas City shows the greatest differences between the BASE simulations and the hygroscopicity sensitivity simulations (red box; Figure 1a). Therefore, the following analysis focuses on the rain event downwind of the urban area (Figure 1a; red box).

During this time period in the focus region, two separate pulses of precipitation occur, the first from 00:00 to 07:00 UTC and second from 12:00 to 17:00 UTC (Figure 3). Prior to 00:00 UTC, the precipitation accumulated over the focus area is small, as are the precipitation differences between the simulations. During the first pulse of precipitation, the BASE simulation accumulates 25 mm of rain. The SULF simulation also accumulates 25 mm, while the ORG, SWITCH and ALL simulations accumulate 27 mm, 28, mm, and 30 mm, respectively (Figure 3). Greater differences between the simulations manifest during the second round of intense precipitation (1200 – 1700 UTC). The BASE simulation accumulates an additional 19 mm, SULF accumulates an addition 25 mm, and the SWITCH and ORG simulations both accumulate an additional 26 mm. The ALL simulation shows the greatest difference in this second pulse and only

accumulates an additional 10 mm of precipitation. Overall, the changes to hygroscopicity affect precipitation patterns and the timing of precipitation, where the second precipitation pulse is influenced by the first pulse.

3.2 Changes in Aerosol Hygroscopicity and Microphysics

We examine the hygroscopicity averaged over the region east of Kansas City (Figure 1a, red box), during the entirety of the intense rain event (0000 – 1800 UTC 5-27-2013) (Figure 4). The probability density functions (PDF) of hygroscopicity changes with each sensitivity simulation, demonstrating that the bulk hygroscopicity distribution is sensitive to changes in individual species' hygroscopicities. While this representation does not tell us about the aerosol particle size, it explains how the bulk hygroscopicity is changing within the focus region. The BASE and SULF simulations hygroscopicity have a peak probability (~15%) at 0.23. While the BASE probability decreases with increasing hygroscopicity values, the SULF simulation decreases more quickly as hygroscopicity increases until 0.33, and then increases to 11% for values above 0.38. The ALL simulation mimics the SULF pattern, though the peak probability is 14% and the slopes are less steep. In the SWITCH simulation, the hygroscopicity probability is lower than the BASE, SULF, and ALL simulations between 0.18 – 0.33, yet higher for larger hygroscopicity values (>0.33). Finally, the ORG simulation shows the most distinct change in hygroscopicity, with a peak probability of 14% for lower hygroscopicity values (0.18). These hygroscopicity changes ultimately lead to differences in accumulated precipitation and the spatial distribution of the precipitation within the focus region (Figures 2 and 3).

Because aerosol hygroscopicity is a key factor in determining how many aerosols will activate as CCN, we hypothesize that hygroscopicity changes will drive changes in the microphysical parameters. To examine this, we evaluate hygroscopicity variations with height during the first and second pulses of precipitation (Figure 5). However, we note that these values should be interpreted carefully, as hygroscopicity is calculated as a function of the interstitial aerosol only, meaning aerosol that has been activated is not included in the calculation. Then, we examine the vertical profiles of hydrometeor size and number during the two precipitation pulses (Figures 6 and 7).

3.2.1 Changes during the first precipitation pulse (00:00-09:00 UTC)

During the first pulse, the lowest hygroscopicity values are near the surface and increase with height until about 6.5km, then decrease with height until 12 km (Figure 5a). At the surface, the ORG simulation has the lowest hygroscopicity of 0.08, while the BASE, SULF, SWITCH, and ALL simulations have similar hygroscopicity values of 0.14. The hygroscopicity differences between these simulations increase at around 1.5 km. At the peak hygroscopicity values around 6 km, the SWITCH simulation shows the greatest hygroscopicity with the ALL simulation showing the lowest hygroscopicity. Again, we note that these results represent the unactiviated or interstitial aerosol.

The SULF simulation has a similar surface hygroscopicity value as the BASE throughout the vertical profile (Figure 5a), yet more cloud drops are activated in this simulation (Figure 6a), resulting in smaller effective radii (Figure 6a). In contrast, the SWITCH and ALL simulations have the smallest number of cloud drops (Figure 6a) with the largest effective radii (Figure 6e). The ORG simulation has fewer cloud drops than

the BASE (and SULF) simulations, but the drop size is comparable to the BASE simulation, larger than the SULF simulation and smaller than the SWITCH and ALL simulations (Figure 6a and 6e). Overall, the hygroscopicity values drive the number and size of the cloud drops, which then influence the formation and size of other hydrometeors. The lower hygroscopicity in the ORG simulation causes fewer cloud drops, the greater hygroscopicity in the SULF simulation causes more aerosols to activate at smaller effective radii, and the SWITCH and ALL simulations have larger and fewer cloud drops (Figure 6a&e), likely driven by the change in ammonium hygroscopicity.

The smaller and more numerous cloud drops in the SULF simulation lead to the fewest number of rain drops (Figure 6b), and a delay in precipitation accumulation (Figure 3). The SWITCH, SULF, and ORG simulations all present initially suppressed precipitation, corresponding to the smaller rain drop effective radii and a less efficient collision and coalescence process. The ALL simulation has the greatest rain drop number concentrations (Figure 6b), and the sizes are similar to the BASE (Figure 6f), where the larger number concentrations increase initial precipitation accumulation (Figure 3).

At higher altitudes in the mixed-phase region of the cloud, the number and size of graupel, ice and snow are affected. The more numerous, smaller cloud drops in the SULF simulation do not autoconvert to rain and freeze as graupel, causing the largest graupel number concentrations (14 L^{-1}; Figure 6c), the ALL graupel radius is larger than the BASE (Figure 6g), due to larger rain and cloud drops freezing. The ALL simulation has the second lowest number concentrations (11 L^{-1}; Figure 6c) and largest sizes of graupel (Figure 6g), corresponding to the larger and more numerous rain drops drops. The ALL simulation dominates the snow number concentrations (16 L^{-1}) (Figure 6d), and has the

largest effective radii (Figure 6h), likely due to enhanced accretion due to larger cloud and rain drop and sizes. The larger graupel and snow hydrometeors accrete more efficiently in the ALL simulation, and melting to larger raindrops, aiding the increased precipitation.

The larger and more numerous hydrometeors in the ALL simulation coincide with the stronger updrafts in the region (Figure 6i), leading to the precipitation increases in this simulation (Figure 3). Conversely, the ORG simulation has the weakest updrafts, which coincides with the smallest, least numerous hydrometeors. The SWITCH and ORG simulation both accumulate more rain than the BASE simulation, but by different microphysical mechanisms. The weaker updrafts in the ORG simulation may not be strong enough to keep the larger hydrometeors aloft, resulting in greater precipitation accumulation. Whereas the SULF simulation has the same amount of accumulated precipitation as the BASE, the updrafts are stronger than the BASE simulation in the coldest regions of the cloud, suggesting the cold production of accumulated precipitation may be compensating for the smaller and more numerous liquid-phase hydrometeors.

3.2.2 Changes during the second precipitation pulse (12:00-17:00 UTC)

In the second pulse, hygroscopicity values are similar near the surface up to about 2km, increasing from about 0.08-0.15 at the surface to 0.5 at around 2km (Figure 5b). The hygroscopicity increase with height suggests an increase in interstitial aerosol, matching the time period when rain accumulation ceases (Figure 3). With increasing height from 6km to 13km, ORG has the smallest hygroscopicity values, and ALL has the greatest values.

519 Because the evolution of the first pulse of precipitation influences the secondary
520 convection, larger changes in hydrometeor size and number occur in the second
521 precipitation pulse (Figure 7). During the second pulse of intense precipitation, the
522 SULF, ORG, and SWITCH simulations all have increased precipitation compared to the
523 BASE simulation during this time period, while the ALL simulation has decreased
524 precipitation (Figure 3). As in the first pulse, cloud drop number concentrations are the
525 greatest in the SULF simulation, the least in the ALL simulation, corresponding to the
526 smallest (SULF) and largest (ALL) effective radii (Figure 7a&e). The SWITCH
527 simulation has the greatest rain drop number concentrations (Figure 7b), which coincides
528 with the largest precipitation enhancement. The ALL simulation has the largest rain
529 drops (Figure 7f), but only one maximum at 4.5 km, whereas the other simulations have a
530 secondary maximum at the lower altitude of 1.5 km. This reflects the number of
531 raindrops reaching the surface as accumulated precipitation, where the SWITCH, SULF,
532 and ORG simulations all have enhanced number concentrations compared to the BASE
533 simulation. The BASE simulation has the fewest rain drops at 4.5 km (Figure 7b). By
534 this time period, the ORG, BASE, and SULF simulations have similar graupel number
535 concentrations (Figure 7c). The SWITCH has the largest graupel hydrometeors,
536 suggesting that melting graupel contributes to the enhanced accumulated precipitation.
537 Whereas the ALL and BASE graupel are approximately the same size, the ALL
538 simulation has the fewest graupel hydrometeors (Figure 7d&h), peaking at the lowest
539 altitude (9 km versus 10 km). As during the first pulse, the ALL simulation has the most
540 snow hydrometeors (Figure 7i), likely persisting from the first pulse of precipitation as a
541 result of relatively small snow hydrometeor fall speeds. The ORG and SWITCH

simulation have the same number concentrations of snow, less than the ALL simulation, but more than SULF and BASE. The ALL snow hydrometeors tend to be larger than all other simulations (Figure 7e).

The ALL simulation also generally has larger cloud (Figure 7e), rain (Figure 7f), and snow (Figure 7h) than the other simulations as well as the strongest downdrafts (Figure 7i). Compared to the BASE, the ORG, SULF, and SWITCH simulations have increased vertical velocities from 1km to 10km (Figure 7i), which accompany the increased precipitation (Figure 3). In the SWITCH simulation, the final pulse yields the largest amount of accumulated rain, which coincides with the greatest number of rain drops (Figure 7b). These increases and decreases in accumulated precipitation suggest that several factors are affected by the changes in hygroscopicities. While large-scale meteorological forcing and local thermodynamic factors are the drivers of this precipitation event, it is clear that chemical composition can affect the intensity of hydrometeor formation and rain rates. Examining the microphysics alone does not fully explain the accumulated precipitation differences, and next we examine cold pools to link the microphysics to the dynamics.

To connect the hygroscopicity to changes in cloud microphysics as demonstrated in Figures 6 and 7, we evaluated the relationships between hygroscopicity and several environmental variables, including aerosol number concentration, vertical velocity, and water vapor mixing ratio (as a proxy for supersaturation). While the relationships between aerosol number concentration and vertical velocities did not vary much between the simulations, the joint probabilities between hygroscopicity and water vapor mixing ratio did show differences between the BASE simulation and four sensitivity tests (Figure

8). In the three simulations that ultimately result in increased precipitation (SWITCH, SULF, and ORG; Figure 8b,d,&e), the probabilities for larger water vapor mixing ratios with respect to hygroscopicities increase. Specifically, the BASE joint probability maximum of 8% occurs at 11 g kg^{-1}, where as for the SWITCH simulation the probability increases to over 10% within the same parameter space. This increase is also consistent in the ORG and SULF simulations. During Phase 2, the distributions broaden for each simulation. However, the increased probability for greater amounts of water vapor persists, and is distributed more evenly among the hygroscopicity values. The increase in water vapor in the SWITCH, ORG, and SULF simulations suggests that the changes to hygroscopicity affect the uptake of water vapor and lead to additional water vapor in these simulations. The increased water vapor could increase instability, which ultimately aids in enhancing precipitation. While this offline analysis indicates that increased water vapor from the hygroscopicity changes leads to the changes in precipitation, a full microphysical budget is required to determine whether evaporation from smaller droplets (as in the SULF simulation) is the cause or if the water is advected. However, the current implementation of the WRF model does not include a budget of the microphysical processes as model output, limiting further attribution of how hygroscopicity affects microphysics.

3.3 Dynamical Effects of Hygroscopicity Changes

Cold pools are evaporatively-cooled regions of downdraft air that spread out horizontally underneath a precipitating cloud (Engerer et al. 2008) and play an important

588 role in squall lines propagation and convective initiation (Rotunno et al. 1988). Cold pool
589 strength is a function of hydrometeor phase change, and hydrometeors are directly
590 affected by aerosol composition (Grant and van den Heever, 2015; Kawecki et al. 2016).
591 Therefore, we examine the impacts the hygroscopicity changes have on the dynamics via
592 the changes to the cold pools. Here we use the methodology described in Kawecki et al,
593 (2016) to examine the cold pool characteristics (Figure 8). During the first pulse there is
594 little difference between BASE and ALL simulations with respect to the cold pool
595 (Figure 8a,b,e&f). However, there is increased area of strong winds in the ALL
596 simulation, indicating more intense precipitation within the region, which corresponds to
597 the increase in accumulated precipitation (Figure 3). At the beginning of the second
598 precipitation pulse at 11:00 UTC, the BASE simulates a strong cold pool entering the
599 sub-region (Figure 8b), while the ALL simulation cold pool encompasses a larger area
600 than the BASE simulation and persists longer, signifying a stronger cold pool (Figure 8e-
601 h). The stronger cold pool corresponds to the stronger downdrafts during this time period
602 (Figure 7i). The larger hydrometeors in the ALL simulation (Figure 6 and 7) lead to
603 initially more precipitation and the stronger and larger cold pool. This enhanced
604 precipitation limits the convective instability and weakens the secondary convection of
605 the second pulse (Figure 3).

606 All three simulations that altered the hygroscopicity of individual species
607 (SWITCH, ORG, and SULF) correspond with enhanced precipitation later in the
608 simulation. This is especially true in the SWITCH simulation, where the final pulse
609 yields the largest amount of accumulated rain. This suggests that several factors are
610 affected by the changes in hygroscopicities. Initial suppression followed by increased

vertical velocities (SULF, ORG) or quicker rainout due to larger drops (Figure 6f) being able to form more quickly (ALL), are both causes for these differences. While large-scale meteorological forcing and local thermodynamic factors are clearly the drivers of this precipitation event, it is clear that chemical composition can affect the intensity of hydrometeor formation and rain rates.

3.4 Evaluation against observed precipitation intensity

To understand the realism of these hygroscopicity sensitivity tests, we compare the PDF of the observed accumulated precipitation values to simulated precipitation in the selected box (Figure 10). We use the Daymet gridded daily precipitation product at 1km resolution (Thornton et al. 2016), which is a high-resolution daily product of precipitation to compare with accumulated precipitation from the five model simulations. Like all gridded datasets, the Daymet dataset has biases. In the Central Plains region, the Daymet dataset captures average precipitation quite well, with a positive bias of less than 0.25 mm (Behnke et al. 2016). However, for events with greater than 100 mm of accumulated precipitation, the Daymet dataset has a negative bias of about 40 mm. While this is actually on the order of 50%, this amount of bias is common with gridded datasets (Behnke et al. 2016).The observed precipitation intensity shows a peak probability at 30 mm, with low probabilities at the lower accumulated values (< 20 mm, 10%) and high accumulated values (< 80 mm, <3%). The NCEP Stage IV gridded dataset has a similar pattern, though it has a greater probability of capturing high-intensity events.

The model simulations show a broad range of accumulated precipitation distributions with several different characteristics than observed (Figure 10). Most of the

cases simulate an increased probability of low intensity (<15 mm) and high intensity (>60 mm) events, and lower frequencies at the center of the precipitation distribution. Of the five simulations, the ALL simulation most closely matches observations, primarily by reducing amount of both low (<15 mm) and high (> 60 mm) precipitation intensities and improving the tail ends of the PDF. While the ALL simulation shifts the observed peak at 35 mm to higher values (50 mm), it reproduces the overall shape of the observed distribution better than the other simulations. The BASE simulation also generally matches the pattern of the observed PDF, yet misses the observed 35 mm peak accumulation and simulates greater values at the distribution tails when compared to the Daymet data. However, when compared to the NCEP Stage-IV data, the BASE simulation closely captures the distribution of the observed high-intensity precipitation events. The ORG simulation diverges from the observed PDF, with a large probability of low-intensity rain events and an increased probability of high-intensity rain events, with the lowest probability of mid-range events. The SULF and SWITCH simulation PDFs are similar, with increases in both low and high-intensity events compared to the observed PDF, and much lower probability of the mid-range events. In the ORG, SWITCH and SULF simulations especially, this pattern indicates that the model is simulating too much rainfall in some grid cells and too little rainfall in others in all simulations. The ALL simulation provides the best evaluation with observations by improving the number of grid cells with the mid-range rain accumulations compared to the other simulations. The changes to the aerosol characteristics via hygroscopicity (Figures 4 and 5) impact the microphysics (Figures 6 and 7), the dynamics (Figure 9), and thus the precipitation patterns and intensity (Figures 2 and 3). By incorporating lower

organic hygroscopicity values and higher hygroscopicity values for sulfate, ammonium and nitrate that depend on the portioning of ammonium, the ALL simulation not only more closely matches the BASE simulation, it also improves the model's ability to represent observed accumulated precipitation.

The improved representation of mid-range intensity precipitation (30 – 60 mm d^{-1}) for this MCS event is a result of how the ALL simulation represents the two pulses of precipitation (May 27, 00:00 –18:00 UTC). By the end of the first pulse, the initially enhanced precipitation leads to a stronger, larger cold pool and suppresses the second pulse of precipitation (Figure 9). As discussed above, the simulations qualitatively agree with the observations although there are some key differences between the observed radar and the simulated radar, as discussed in Kawecki et al. (2016). While the ALL simulation shows better agreement with the observations, we note that there are some discrepancies with the storm placement that may influence the evaluation of the accumulated precipitation.

4.0 Discussion and Conclusions

We test the default hygroscopicity values in WRF-Chem during a mesoscale convective system event to understand the role of the hygroscopicity parameterization on the simulation of high intensity rainfall. We find that updating the model parameters to laboratory-derived values and including a switch to account for changes in ammonium hygroscopicity based on partitioning can influence the spatial patterns of precipitation and the location of precipitation intensity. Changing hygroscopicity for individual aerosol species alters the accumulation mode bulk hygroscopicity distributions, and these

distribution differences drive changes in microphysical characteristics (hydrometeor number concentrations and sizes) that alter rainfall duration and intensity. The largest contiguous area of rainfall amounts greater than 100 mm exists in the SWITCH case, which implies that including the larger hygroscopicity values for ammonium and nitrate could impact the simulation of storm severity and flooding. Compared to the observations of daily-accumulated precipitation, the model evaluation improves when all lab-derived hygroscopicities are included, with the caveat that the gridded dataset has a large negative bias compared to point observations, and may miss the most extreme precipitation events. Additionally, even though the simulated aerosol mass qualitatively agrees with observations, errors in the simulated aerosol are likely confounded with hygroscopicity changes, and the same improvement in precipitation may not hold for other events and model simulations.

Although there were notable spatial differences of accumulated precipitation between the simulations, the overall domain average accumulated precipitation are similar (e.g., variations of less than 15%). Therefore, including updated aerosol hygroscopicity may not necessarily improve a regional forecast but may improve the placement and frequency of intense precipitation. This spatial redistribution of high-intensity precipitation when altering aerosol hygroscopicity values emphasizes the need for mesoscale models to account for chemical composition coupled with microphysics and thermodynamics, thereby enabling the chemistry-meteorology feedbacks that control the spatial distribution of the precipitation.

While including more complex representations of aerosol activation as CCN aims to more closely represent real-world environments, there are limitations in our model

simulations. First, the activation of aerosols as CCN does not account for interactions on the aerosol surface. While the modal and bin representations of aerosol size assume internally mixed modes and bins, individual aerosols are highly complex, and cannot accurately account for ageing processes in the atmosphere. Even though the hygroscopicity is a good metric for activating aerosols that are mostly inorganic (e.g., ammonium sulfate, ammonium nitrate, salts), it has trouble representing activation of aerosols that are mixtures of organic and inorganic species (Good et al. 2010). Often the kappa method will activate these mixtures at smaller diameters than actually observed, potentially due to heterogeneous surface interactions where surface tension increases linearly with decreasing surface concentration (Ruehl et al. 2016).

Additionally, the 4km horizontal grid spacing for the simulation implemented in these simulations likely simulates weaker updrafts and downdrafts than actual updrafts and downdrafts. This is important to note because aerosol activation as cloud drops depends on updraft speeds in addition to hygroscopicity and supersaturation. Therefore, the results of this particular work may not translate across all spatial scales. Furthermore, we examine a region with a relatively balanced mix of aerosol types (organic and inorganic). We recognize that in different regions, aerosol types may not be as evenly distributed, where changes to hygroscopicity values may have a relatively large or small effect. For example, in a region dominated by organic aerosol, changing the hygroscopicity of the sulfate aerosol species would have little effect. Finally, different microphysics schemes can strongly influence precipitation intensity, and we did not test the hygroscopicity effects with different microphysics schemes. Therefore, the changes in precipitation demonstrated between simulations may not be consistent between different

physics parameterizations. Finally, a major model limitation is the lack of a full microphysical budget. This limitation prevents a full analysis of how hygroscopicity changes ultimately influence precipitation amounts.

Even with these limitations, moving towards a more realistic modeling approach is necessary in understanding potential changes in precipitation patterns as a result of current and future heterogeneity of aerosol sources. For example, (Saide et al. 2016) found that using a bulk hygroscopicity value of 0.4 for all aerosols potentially changes the significant tornado parameter, which has implications for severe weather. Additionally, the implemented switch is based solely on the ratio of ammonium to sulfate. In regions with relatively large amounts of nitrate and sulfate, such as urban regions, this may misrepresent ammonium hygroscopicity and therefore lead to unrealistic changes in the microphysics and precipitation patterns. The current microphysics implementation does not include aerosols as ice nuclei, which can impact the radiative balance within deep convection (Fan et al. 2013). We note this is important, especially for dust, which is documented as efficient ice nuclei (DeMott et al. 2003). While this study focused primarily on the liquid phase, the solid phase has been shown to affect precipitation processes and total rainfall amounts (Cheng et al. 2010).

Overall, these results suggest that the model treatment of aerosol composition via the hygroscopicity parameter can affect short-term weather and the simulation of high intensity events. Including updated hygroscopicity values leads to different realizations of high intensity precipitation events, and may improve the simulation of these types of precipitation events. These differences suggest that aerosol hygroscopicity be evaluated more closely in future model studies in regions with varying aerosol compositions.

Acknowledgements

Funding for this research was provided by the NASA Interdisciplinary Science program through Project NNX12AM89G: "Storms, forms, and complexity of the urban canopy: How land use, settlement patterns, and the shapes of cities influence severe weather," the National Science Foundation grant 1313897, and the Elizabeth Caroline Crosby Grant.

Model simulations from this manuscript are available from the University of Michigan Deep Blue data archive:

https://deepblue.lib.umich.edu/data/concern/generic_works/cr56n1028?locale=en .

References

Abdul - Razzak, H., and S. J. Ghan, 2000: A parameterization of aerosol activation: 2. Multiple aerosol types. *Journal of Geophysical Research: Atmospheres*, **105,** 6837-6844.

Ackerman, A. S., O. Toon, D. Stevens, A. Heymsfield, V. Ramanathan, and E. Welton, 2000: Reduction of tropical cloudiness by soot. *Science*, **288,** 1042-1047.

Ackermann, I. J., H. Hass, M. Memmesheimer, A. Ebel, F. S. Binkowski, and U. Shankar, 1998: Modal aerosol dynamics model for Europe: Development and first applications. *Atmospheric environment*, **32,** 2981-2999 %@ 1352-2310.

Albrecht, B. A., 1989: Aerosols, cloud microphysics, and fractional cloudiness. *Science*, **245,** 1227-1230.

Andreae, M., and A. Gelencsér, 2006: Black carbon or brown carbon? The nature of light-absorbing carbonaceous aerosols. *Atmospheric Chemistry and Physics*, **6,** 3131-3148.

Andreae, M. O., D. Rosenfeld, P. Artaxo, A. Costa, G. Frank, K. Longo, and M. Silva-Dias, 2004: Smoking rain clouds over the Amazon. *science*, **303,** 1337-1342.

Behera, S. N., M. Sharma, V. P. Aneja, and R. Balasubramanian, 2013: Ammonia in the atmosphere: a review on emission sources, atmospheric chemistry and deposition on terrestrial bodies. *Environmental Science and Pollution Research*, **20,** 8092-8131 %@ 0944-1344.

Behnke, R., S. Vavrus, A. Allstadt, T. Albright, W. E. Thogmartin, and V. C. Radeloff, 2016: Evaluation of downscaled, gridded climate data for the conterminous United States. *Ecological Applications*.

Boucher, O., and Coauthors, 2013: Clouds and aerosols. *Climate change 2013: the physical science basis. Contribution of Working Group I to the Fifth Assessment Report of the Intergovernmental Panel on Climate Change*, Cambridge University Press, 571-657.

Butler, T., F. Vermeylen, C. M. Lehmann, G. E. Likens, and M. Puchalski, 2016: Increasing ammonia concentration trends in large regions of the USA derived from the NADP/AMoN network. *Atmospheric Environment %@ 1352-2310*.

Carrió, G. G., W. R. Cotton, and W. Y. Y. Cheng, 2010: Urban growth and aerosol effects on convection over Houston. *Atmospheric Research*, **96,** 560-574.

Cerully, K. M., and Coauthors, 2015: On the link between hygroscopicity, volatility, and oxidation state of ambient and water-soluble aerosols in the southeastern United States. *Atmospheric Chemistry and Physics*, **15,** 8679-8694.

Chapman, E. G., W. Gustafson Jr, R. C. Easter, J. C. Barnard, S. J. Ghan, M. S. Pekour, and J. D. Fast, 2009: Coupling aerosol-cloud-radiative processes in the WRF-Chem model: Investigating the radiative impact of elevated point sources. *Atmospheric Chemistry and Physics*, **9,** 945-964.

Cheng, C.-T., W.-C. Wang, and J.-P. Chen, 2010: Simulation of the effects of increasing cloud condensation nuclei on mixed-phase clouds and precipitation of a front system. *Atmospheric Research*, **96,** 461-476.

DeMott, P. J., and Coauthors, 2003: African dust aerosols as atmospheric ice nuclei. *Geophysical Research Letters*, **30**.
Dudhia, J., 1996: Back to basics: thunderstorms: Part 1. *Weather*, **51,** 371-376.
Dusek, U., and Coauthors, 2006: Size matters more than chemistry for cloud-nucleating ability of aerosol particles. *Science*, **312,** 1375-1378 %@ 0036-8075.
Easter, R. C., and P. V. Hobbs, 1974: The formation of sulfates and the enhancement of cloud condensation nuclei in clouds. *Journal of the Atmospheric Sciences*, **31,** 1586-1594 %@ 1520-0469.
Eidhammer, T., M. C. Barth, M. D. Petters, C. Wiedinmyer, and A. J. Prenni, 2014: Aerosol microphysical impact on summertime convective precipitation in the Rocky Mountain region. *Journal of Geophysical Research: Atmospheres*, **119,** 11,709-711,728.
Ek, M., and Coauthors, 2003: Implementation of Noah land surface model advances in the National Centers for Environmental Prediction operational mesoscale Eta model. *Journal of Geophysical Research: Atmospheres*, **108**.
Ekman, A., C. Wang, J. Wilson, and J. Ström, 2004: Explicit simulations of aerosol physics in a cloud-resolving model: a sensitivity study based on an observed convective cloud. *Atmospheric Chemistry and Physics*, **4,** 773-791.
Emmons, L., and Coauthors, 2010: Description and evaluation of the Model for Ozone and Related chemical Tracers, version 4 (MOZART-4). *Geoscientific Model Development*, **3,** 43-67.
EPA, 2011: National Emissions Inventory.
Fan, J., Y. Wang, D. Rosenfeld, and X. Liu, 2016: Review of Aerosol–Cloud Interactions: Mechanisms, Significance, and Challenges. *Journal of the Atmospheric Sciences*, **73,** 4221-4252.
Fan, J., R. Zhang, G. Li, W. K. Tao, and X. Li, 2007: Simulations of cumulus clouds using a spectral microphysics cloud - resolving model. *Journal of Geophysical Research: Atmospheres*, **112**.
Fan, J., D. Rosenfeld, Y. Ding, L. R. Leung, and Z. Li, 2012: Potential aerosol indirect effects on atmospheric circulation and radiative forcing through deep convection. *Geophysical Research Letters*, **39**.
Fan, J., D. Rosenfeld, Y. Yang, C. Zhao, L. R. Leung, and Z. Li, 2015: Substantial contribution of anthropogenic air pollution to catastrophic floods in Southwest China. *Geophysical Research Letters*, **42,** 6066-6075.
Fan, J., L. R. Leung, D. Rosenfeld, Q. Chen, Z. Li, J. Zhang, and H. Yan, 2013: Microphysical effects determine macrophysical response for aerosol impacts on deep convective clouds. *Proc Natl Acad Sci U S A*, **110,** E4581-4590.
Ghan, S. J., and S. E. Schwartz, 2007: Aerosol properties and processes. *Bulletin of the American Meteorological Society*, **88,** 1059.
Good, N., and Coauthors, 2010: Consistency between parameterisations of aerosol hygroscopicity and CCN activity during the RHaMBLe discovery cruise. *Atmospheric Chemistry and Physics*, **10,** 3189-3203.
Grell, G. A., S. E. Peckham, R. Schmitz, S. A. McKeen, G. Frost, W. C. Skamarock, and B. Eder, 2005: Fully coupled "online" chemistry within the WRF model. *Atmospheric Environment*, **39,** 6957-6975.

Guenther, A., T. Karl, P. Harley, C. Wiedinmyer, P. Palmer, and C. Geron, 2006: Estimates of global terrestrial isoprene emissions using MEGAN (Model of Emissions of Gases and Aerosols from Nature). *Atmospheric Chemistry and Physics Discussions*, **6,** 107-173.

Hand, J., B. Schichtel, W. Malm, and M. Pitchford, 2012: Particulate sulfate ion concentration and SO 2 emission trends in the United States from the early 1990s through 2010. *Atmospheric Chemistry and Physics*, **12,** 10353-10365.

Hong, S.-Y., Y. Noh, and J. Dudhia, 2006: A new vertical diffusion package with an explicit treatment of entrainment processes. *Monthly Weather Review*, **134,** 2318-2341.

Houze, R. A., 2004: Mesoscale convective systems. *Reviews of Geophysics*, **42**.

Kawecki, S., G. M. Henebry, and A. L. Steiner, 2016: Effects of Urban Plume Aerosols on a Mesoscale Convective System. *Journal of the Atmospheric Sciences*, **73,** 4641-4660 %@ 0022-4928.

Khain, A., M. Ovtchinnikov, M. Pinsky, A. Pokrovsky, and H. Krugliak, 2000: Notes on the state-of-the-art numerical modeling of cloud microphysics. *Atmospheric Research*, **55,** 159-224.

Khain, A., and Coauthors, 2015: Representation of microphysical processes in cloud - resolving models: Spectral (bin) microphysics versus bulk parameterization. *Reviews of Geophysics*, **53,** 247-322.

Köhler, H., 1936: The nucleus in and the growth of hygroscopic droplets. *Transactions of the Faraday Society*, **32,** 1152-1161.

Kulmala, M., A. Laaksonen, and L. Pirjola, 1998: Parameterizations for sulfuric acid/water nucleation rates. *Journal of Geophysical Research: Atmospheres*, **103,** 8301-8307 %@ 2156-2202.

Lebo, Z. J., and J. H. Seinfeld, 2011: Theoretical basis for convective invigoration due to increased aerosol concentration. *Atmospheric Chemistry and Physics*, **11,** 5407-5429.

Lin, Y. 2011. GCIP/EOP Surface: Precipitation NCEP/EMC 4KM Gridded Data (GRIB) Stage IV Data. Version 1.0. UCAR/NCAR - Earth Observing Laboratory. https://doi.org/10.5065/D6PG1QDD. Accessed 14 May 2017.

Malm, W. C., J. F. Sisler, D. Huffman, R. A. Eldred, and T. A. Cahill, 1994: Spatial and seasonal trends in particle concentration and optical extinction in the United States. *Journal of Geophysical Research: Atmospheres*, **99,** 1347-1370.

Marinescu, P., S. Heever, S. Saleeby, and S. Kreidenweis, 2016: The microphysical contributions to and evolution of latent heating profiles in two MC3E MCSs. *Journal of Geophysical Research: Atmospheres*, **121,** 7913-7935.

Morrison, H., J. Curry, and V. Khvorostyanov, 2005: A new double-moment microphysics parameterization for application in cloud and climate models. Part I: Description. *Journal of the Atmospheric Sciences*, **62,** 1665-1677.

NCEI, 2013: North American Model-Reanalysis, 6-hourly dataset. NCEI, Ed., http://nomads.ncdc.noaa.gov/data/namanl/201305/.

Ntelekos, A. A., J. A. Smith, L. Donner, J. D. Fast, W. I. Gustafson, E. G. Chapman, and W. F. Krajewski, 2009: The effects of aerosols on intense convective precipitation in

the northeastern United States. *Quarterly Journal of the Royal Meteorological Society*, **135,** 1367-1391.
Petters, M. D., and S. M. Kreidenweis, 2007: A single parameter representation of hygroscopic growth and cloud condensation nucleus activity. *Atmospheric Chemistry and Physics*, **7,** 1961-1971 %@ 1680-7316.
Petters, M. D., and Coauthors, 2009: Towards closing the gap between hygroscopic growth and activation for secondary organic aerosol–Part 2: Theoretical approaches. *Atmospheric Chemistry and Physics*, **9,** 3999-4009 %@ 1680-7316.
Pielke, R. A., and Coauthors, 1992: A comprehensive meteorological modeling system—RAMS. *Meteorology and Atmospheric Physics*, **49,** 69-91 %@ 0177-7971.
Price, E., J. Mielikainen, M. Huang, B. Huang, H.-L. A. Huang, and T. Lee, 2014: GPU-accelerated longwave radiation scheme of the Rapid Radiative Transfer Model for General Circulation Models (RRTMG). *IEEE Journal of Selected Topics in Applied Earth Observations and Remote Sensing*, **7,** 3660-3667 %@ 1939-1404.
Raymond, T. M., and S. N. Pandis, 2002: Cloud activation of single - component organic aerosol particles. *Journal of Geophysical Research: Atmospheres*, **107**.
Rosenfeld, D., 2000: Suppression of rain and snow by urban and industrial air pollution. *Science*, **287,** 1793-1796.
Rosenfeld, D., and Coauthors, 2008: Flood or drought: how do aerosols affect precipitation? *science*, **321,** 1309-1313.
Rosenfeld, D., and Coauthors, 2014: Global observations of aerosol - cloud - precipitation - climate interactions. *Reviews of Geophysics*, **52,** 750-808.
Ruehl, C. R., J. F. Davies, and K. R. Wilson, 2016: An interfacial mechanism for cloud droplet formation on organic aerosols. *Science*, **351,** 1447-1450 %@ 0036-8075.
Saide, P. E., G. Thompson, T. Eidhammer, A. M. Silva, R. B. Pierce, and G. R. Carmichael, 2016: Assessment of biomass burning smoke influence on environmental conditions for multiyear tornado outbreaks by combining aerosol - aware microphysics and fire emission constraints. *Journal of Geophysical Research: Atmospheres*, **121**.
Saide, P. E., and Coauthors, 2015: Central American biomass burning smoke can increase tornado severity in the U.S. *Geophysical Research Letters*, **42,** 956-965.
Saleeby, S., S. Heever, P. Marinescu, S. Kreidenweis, and P. DeMott, 2016: Aerosol effects on the anvil characteristics of mesoscale convective systems. *Journal of Geophysical Research: Atmospheres*, **121**.
Saleeby, S. M., S. R. Herbener, S. C. van den Heever, and T. L'Ecuyer, 2015: Impacts of cloud droplet–nucleating aerosols on shallow tropical convection. *Journal of the Atmospheric Sciences*, **72,** 1369-1385.
Sheffield, Amanda M., Stephen M. Saleeby, and Susan C. Heever, 2015: Aerosol-induced mechanisms for cumulus congestus growth. *Journal of Geophysical Research: Atmospheres* **120**, 8941-8952.
Schell, B., I. J. Ackermann, H. Hass, F. S. Binkowski, and A. Ebel, 2001: Modeling the formation of secondary organic aerosol within a comprehensive air quality model system. *Journal of Geophysical Research: Atmospheres*, **106,** 28275-28293.

933 Smith, A. B., and R. W. Katz, 2013: US billion-dollar weather and climate disasters:
934 data sources, trends, accuracy and biases. *Natural hazards*, **67,** 387-410 %@ 0921-
935 0030X.
936 Stevens, B., and G. Feingold, 2009: Untangling aerosol effects on clouds and
937 precipitation in a buffered system. *Nature*, **461,** 607-613.
938 Stockwell, W. R., P. Middleton, J. S. Chang, and X. Tang, 1990: The second generation
939 regional acid deposition model chemical mechanism for regional air quality
940 modeling. *Journal of Geophysical Research: Atmospheres (1984–2012)*, **95,** 16343-
941 16367.
942 Storelvmo, T., and I. Tan, 2015: The Wegener-Bergeron-Findeisen process–Its
943 discovery and vital importance for weather and climate. *Meteor. Z*, **24,** 455-461.
944 Tao, W.-K., J.-P. Chen, Z. Li, C. Wang, and C. Zhang, 2012: Impact of aerosols on
945 convective clouds and precipitation. *Reviews of Geophysics*, **50**.
946 Thornton, P. E., M. M. Thornton, and R. S. Vose, 2016: Daymet V3: Annual Tile
947 Summary Cross-Validation Statistics for North America, Hawaii. ORNL DAAC, Oak
948 Ridge, Tennessee, USA.
949 Twomey, S., 1977: The influence of pollution on the shortwave albedo of clouds.
950 *Journal of the atmospheric sciences*, **34,** 1149-1152.
951 van den Heever, S. C., and W. R. Cotton, 2007: Urban Aerosol Impacts on Downwind
952 Convective Storms. *Journal of Applied Meteorology and Climatology*, **46,** 828-850.
953 Van den Heever, S. C., G. G. Carrió, W. R. Cotton, P. J. DeMott, and A. J. Prenni, 2006:
954 Impacts of nucleating aerosol on Florida storms. Part I: Mesoscale simulations.
955 *Journal of the atmospheric sciences*, **63,** 1752-1775.
956 VanReken, T. M., N. L. Ng, R. C. Flagan, and J. H. Seinfeld, 2005: Cloud condensation
957 nucleus activation properties of biogenic secondary organic aerosol. *Journal of*
958 *Geophysical Research: Atmospheres*, **110**.
959 Virkkula, A., R. Van Dingenen, F. Raes, and J. Hjorth, 1999: Hygroscopic properties of
960 aerosol formed by oxidation of limonene, α - pinene, and β - pinene. *Journal of*
961 *Geophysical Research: Atmospheres*, **104,** 3569-3579 %@ 2156-2202.
962 Wang, J., S. C. van den Heever, and J. S. Reid, 2009: A conceptual model for the link
963 between Central American biomass burning aerosols and severe weather over the
964 south central United States. *Environmental Research Letters*, **4,** 015003.
965 Ward, D., and W. Cotton, 2011: A Method for Forecasting Cloud Condensation Nuclei
966 Using Predictions of Aerosol Physical and Chemical Properties from WRF/Chem.
967 *Journal of Applied Meteorology and Climatology*, **50,** 1601-1615.
968 Wild, O., X. Zhu, and M. J. Prather, 2000: Fast-J: Accurate simulation of in-and below-
969 cloud photolysis in tropospheric chemical models. *Journal of Atmospheric Chemistry*,
970 **37,** 245-282.
971 Zhang, J., J. S. Reid, M. Christensen, and A. Benedetti, 2016: An evaluation of the
972 impact of aerosol particles on weather forecasts from a biomass burning aerosol
973 event over the Midwestern United States: observational-based analysis of surface
974 temperature. *Atmospheric Chemistry and Physics*, **16,** 6475-6494.
975

976

977

978

979 ***Figure 1:*** a) BASE case boundary layer (0-2 km), 24 hour averaged (5-26 06:00 UTC to
980 5-27 06:00 UTC) total PM 2.5 ($\mu g\ m^{-3}$). IMPROVE (solid) and modeled (hatched)
981 speciated aerosol for b) Lake Seguma, IA (LAKE) and c) El Dorado Springs, MO (EDS).
982 IMPROVE data is the average of May 22 and 25 2013 samples and modeled data is the
983 boundary layer average of a 3x3 grid cell average of 144 km^2 region containing the
984 location of the site. d) Modeled speciated aerosol east of Kansas City in the region of
985 high precipitation (denoted by the red box in Figure 1a).

986

987 ***Figure 2:*** Accumulated precipitation for the 24 hour period ending on 5-27 at 18:00 UTC
988 for the a) NCEP Stage IV observed, b) BASE, c) SULF, d) ORG , e) SWITCH and f)
989 ALL simulations. Frequency of heavy rain (< 10 mm/hour) occurring over the same 24
990 hour period for the g) BASE, h) SULF, i) ORG, j) SWITCH, and k) ALL simulations.
991 The red box in Figure 1a indicates the analysis region in Figures 3-5.

992

993 ***Figure 3:*** Area averaged (red box: Figure2a) accumulated precipitation from May 27
994 00:00 -18:00 UTC, for NCEP Stage IV precipitation retrieval (dashed black line), BASE
995 (solid black line), SULF (red line), ORG (green line), SWITCH (blue line), and ALL
996 (gray line) simulations.

997

998 ***Figure 4:*** Probability distribution functions (PDFs) for the five simulations (BASE,
999 SULF, ORG, SWITCH, ALL) for Accumulation mode bulk hygroscopicity. PDFs are

1000 computed based on the time period ranging from 0000 –1800 UTC, 5-27-2013 in the red
1001 box denoted in Figure 2a.
1002
1003 ***Figure 5:*** Area averaged (red box; Figure 2a) vertical profiles of accumulation-mode
1004 hygroscopicity temporally averaged from a) 0000 – 0900 UTC (Pulse 1) and b) 1000 –
1005 1800 UTC (Pulse 2), for the BASE (black line), SULF (red line), ORG (green line),
1006 SWITCH (blue line), and ALL (gray line) simulations.
1007
1008 ***Figure 6***: Area averaged (red box; Figure 2a) vertical profiles during Pulse 1 (0000 –
1009 0900 UTC). The first column are the number concentrations (# kg -1) for a) cloud drops
1010 b) raindrops, c) graupel, and d) snow. The second column has the effective radii for e)
1011 cloud drop, f) raindrops, g) graupel, and h) snow, and the i) vertical velocity (m s-1).
1012 Simulations are denoted by colors: for BASE (black line), SWITCH (blue line), ALL
1013 (gray line), ORG (green line), and SULF (red line) simulations.
1014
1015 ***Figure 7:*** Same as Figure 6, except for the time period 10:00 – 18:00 UTC.
1016
1017 ***Figure 8:*** Bivariate probability density function of hygroscopicity and water vapor
1018 mixing ratio in g kg^{-1} for phase 1 (a-e), and phase 2 (f-j) for each simulation.
1019
1020 ***Figure 9:*** 10- meter maximum wind speed (12 m s^{-1} contour; solid black line) and the
1021 lowest level perturbation temperature (K; blue (negative) and red (positive) contours) for

BASE simulation (a-d) and the ALL simulation (e-h). The black dots indicate the location of Kansas City, MO.

Figure 10: Probability density function (PDF) of observed (grey) and modeled (BASE-black, SULF-red, ORG-green, SWITCH-blue, ALL – black dashed) 24-hour accumulated precipitation calculated over the red box denoted in Figure 2a.

Aerosol Species	WRF-Chem Value	Ward & Cotton
SO_4^{-2}	0.5	0.71
NO_3^-	0.5	0.51
NH_4^+ (SO_4)	0.5	0.61
NH_4^+ (NO_3)	0.5	0.67
Antha	0.14	0.3
OIN	0.14	N/A
orgaro1	0.14	0.051
orgaro2	0.14	0.094
orgalk	0.14	0.005
orgole	0.14	0.19
orgba1	0.14	0.10
orgba2	0.14	0.10
orgba3	0.14	0.08
orgba4	0.14	0.08
orgpa (orgoin)	0.14	0.073
ec	1.0 x 10-6	0.02
seasalt	1.16	1.28
soila	0.1	0.04

Table 1: Hygroscopicity values assigned for aerosol species in the MADE/SORGAM WRF-Chem version 3.6 and the values assigned in Ward and Cotton (2011).

Figures

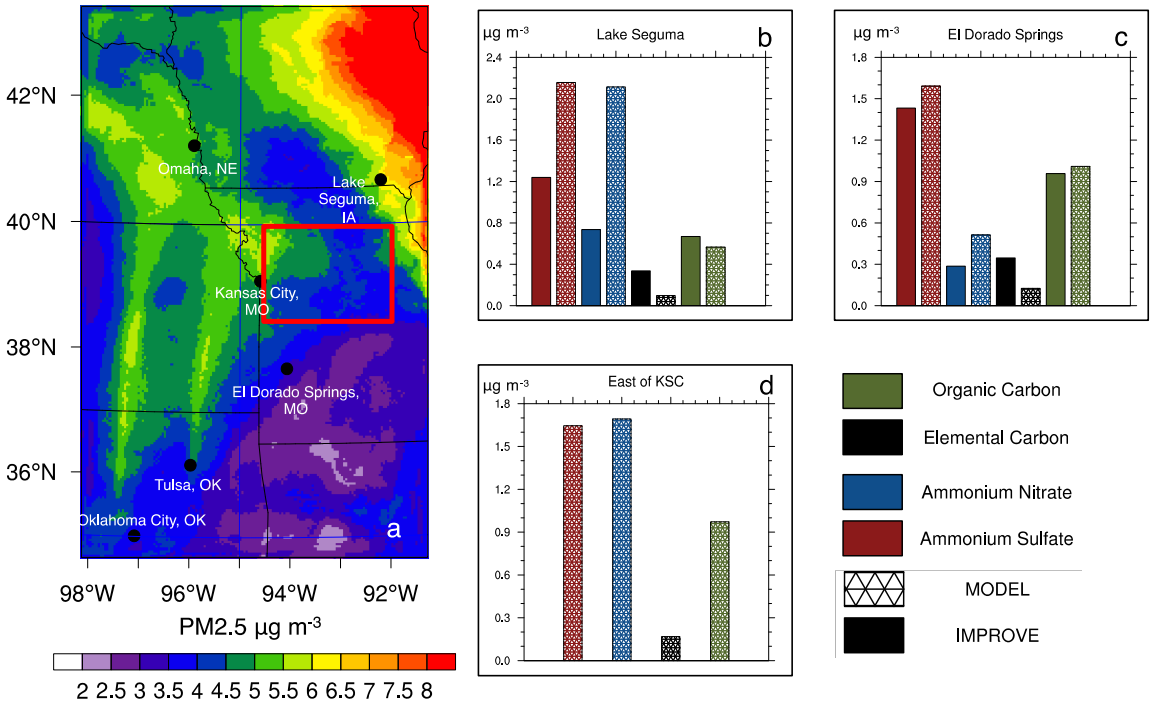

Figure 1: a) BASE case boundary layer (0-2 km), 24 hour averaged (5-26 06:00 UTC to 5-27 06:00 UTC) total PM 2.5 (µg m^{-3}). IMPROVE (solid) and modeled (hatched) speciated aerosol for b) Lake Seguma, IA (LAKE) and c) El Dorado Springs, MO (EDS). IMPROVE data is the average of May 22 and 25 2013 samples and modeled data is the boundary layer average of a 3x3 grid cell average of 144 km^2 region containing the location of the site. d) Modeled speciated aerosol east of Kansas City in the region of high precipitation (denoted by the red box in Figure 1a).

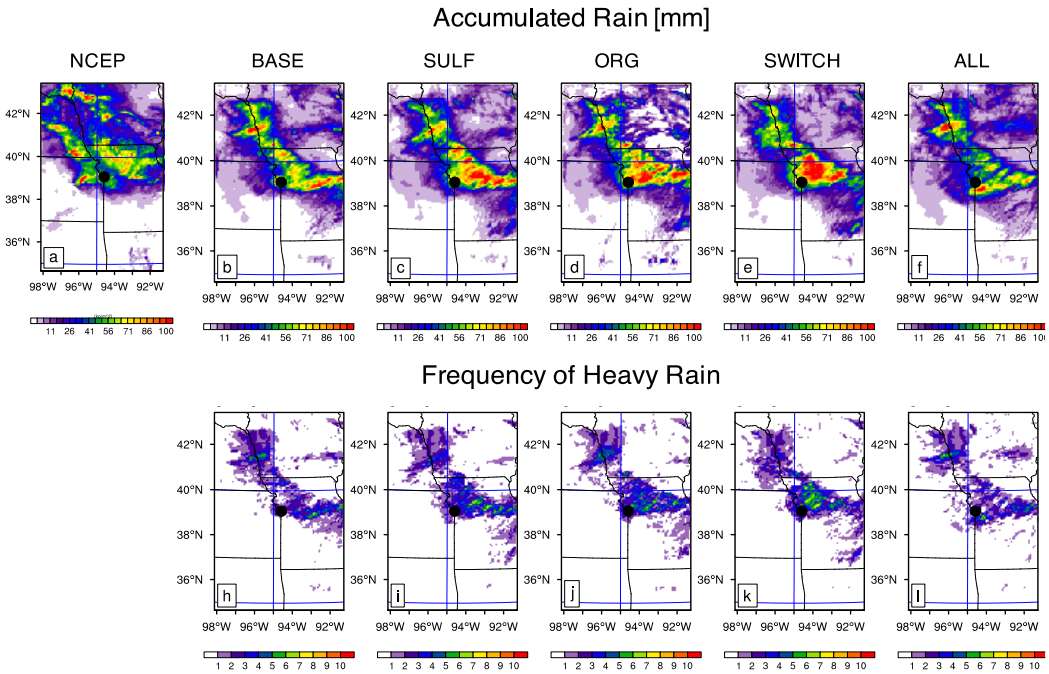

1061

1062 ***Figure 2:*** Accumulated precipitation for the 24 hour period ending on 5-27 at 18:00 UTC

1063 for the a) NCEP Stage IV observed, b) BASE, c) SULF, d) ORG , e) SWITCH and f)

1064 ALL simulations. Frequency of heavy rain (< 10 mm/hour) occurring over the same 24

1065 hour period for the g) BASE, h) SULF, i) ORG, j) SWITCH, and k) ALL simulations.

1066 The red box in Figure 1a indicates the analysis region in Figures 3-5.

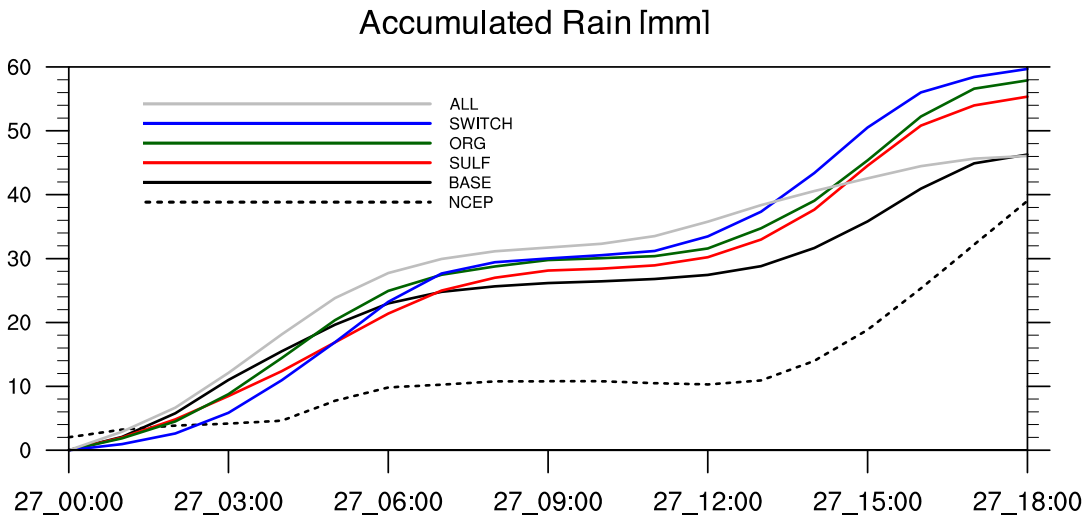

Figure 3: Area averaged (red box: Figure2a) accumulated precipitation from May 27 00:00 -18:00 UTC, for NCEP Stage IV precipitation retrieval (dashed black line), BASE (solid black line), SULF (red line), ORG (green line), SWITCH (blue line), and ALL (gray line) simulations.

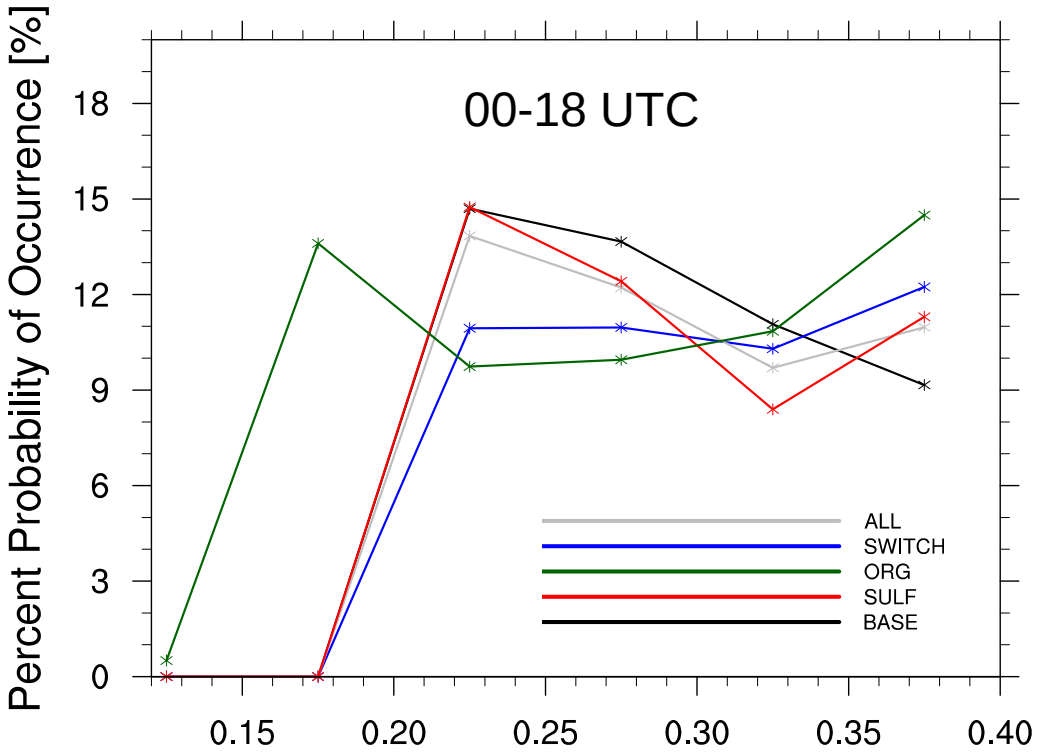

Figure 4: Probability distribution functions (PDFs) for the five simulations (BASE, SULF, ORG, SWITCH, ALL) for Accumulation mode bulk hygroscopicity. PDFs are computed based on the time period ranging from 0000 –1800 UTC, 5-27-2013 in the red box denoted in Figure 2a.

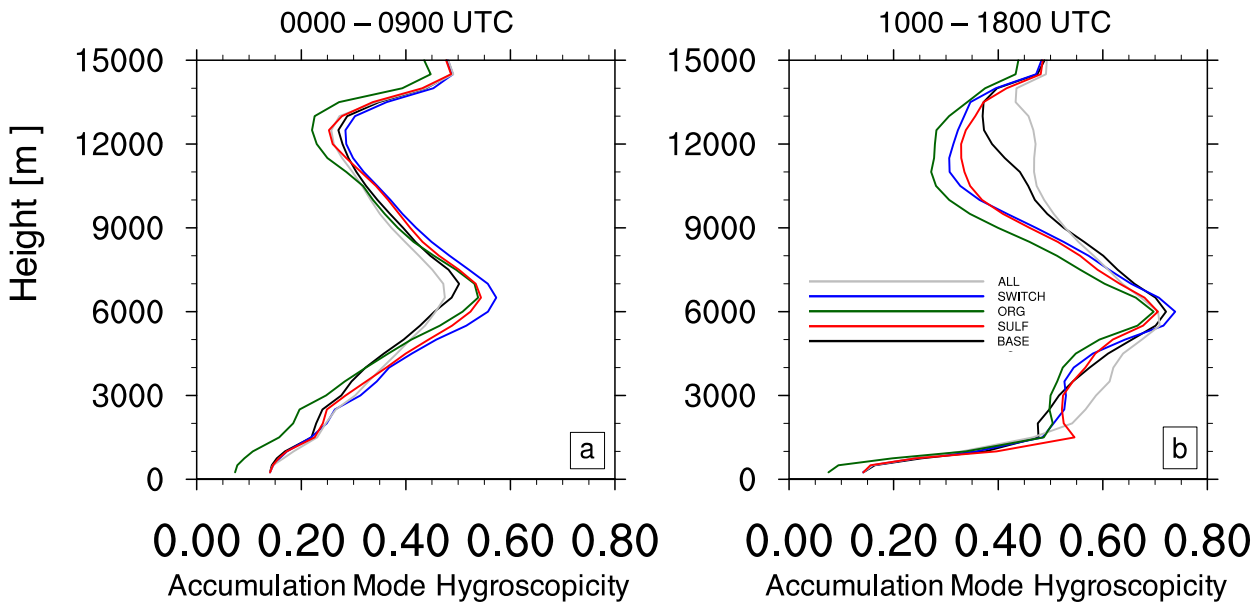

Figure 5: Area averaged (red box; Figure 2a) vertical profiles of accumulation-mode hygroscopicity temporally averaged from a) 0000 – 0900 UTC (Pulse 1) and b) 1000 – 1800 UTC (Pulse 2), for the BASE (black line), SULF (red line), ORG (green line), SWITCH (blue line), and ALL (gray line) simulations.

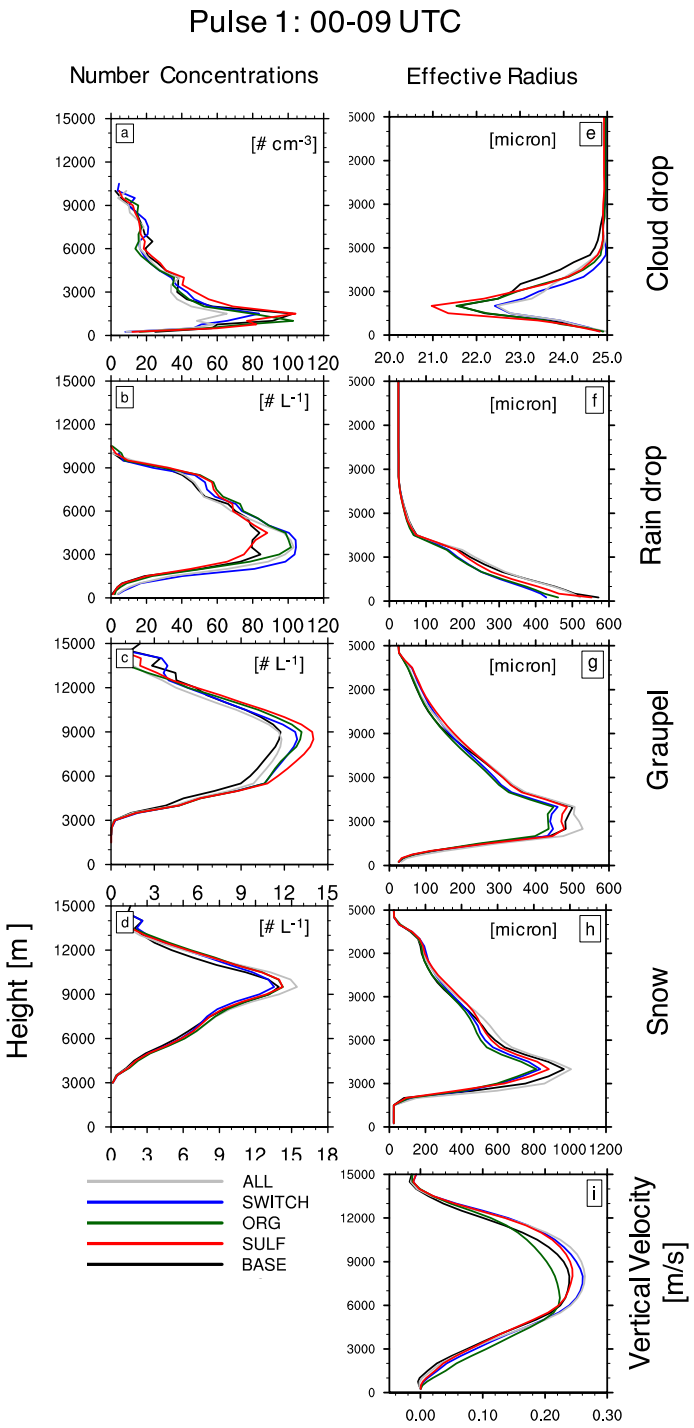

Figure 6: Area averaged (red box; Figure 2a) vertical profiles during Pulse 1 (0000 – 0900 UTC). The first column are the number concentrations (# kg -1) for a) cloud drops b) raindrops, c) graupel, and d) snow. The second column has the e) vertical velocity (m

1104 s-1) and effective radii for f) cloud drop, g) raindrops, h) graupel, and i) snow.

1105 Simulations are denoted by colors: for BASE (black line), SWITCH (blue line), ALL

1106 (gray line), ORG (green line), and SULF (red line) simulations.

1107

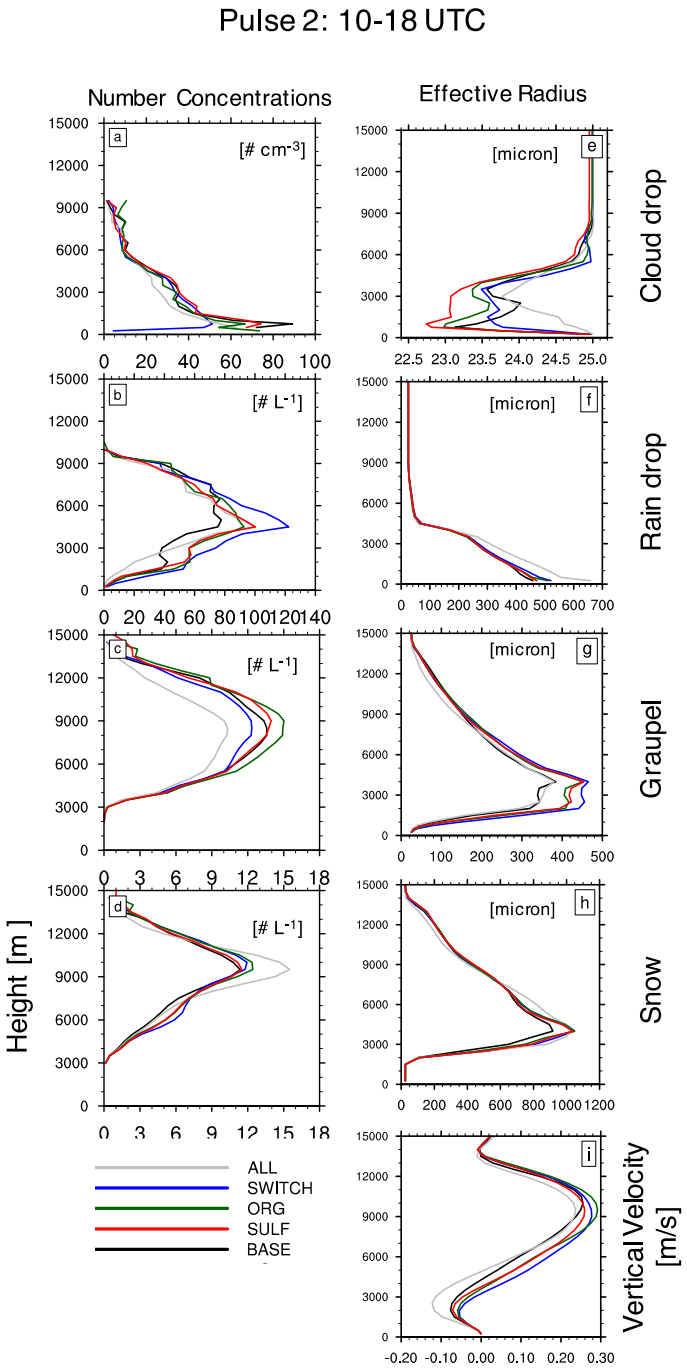

Figure 7: Same as Figure 6, except for the time period 10:00 – 18:00 UTC.

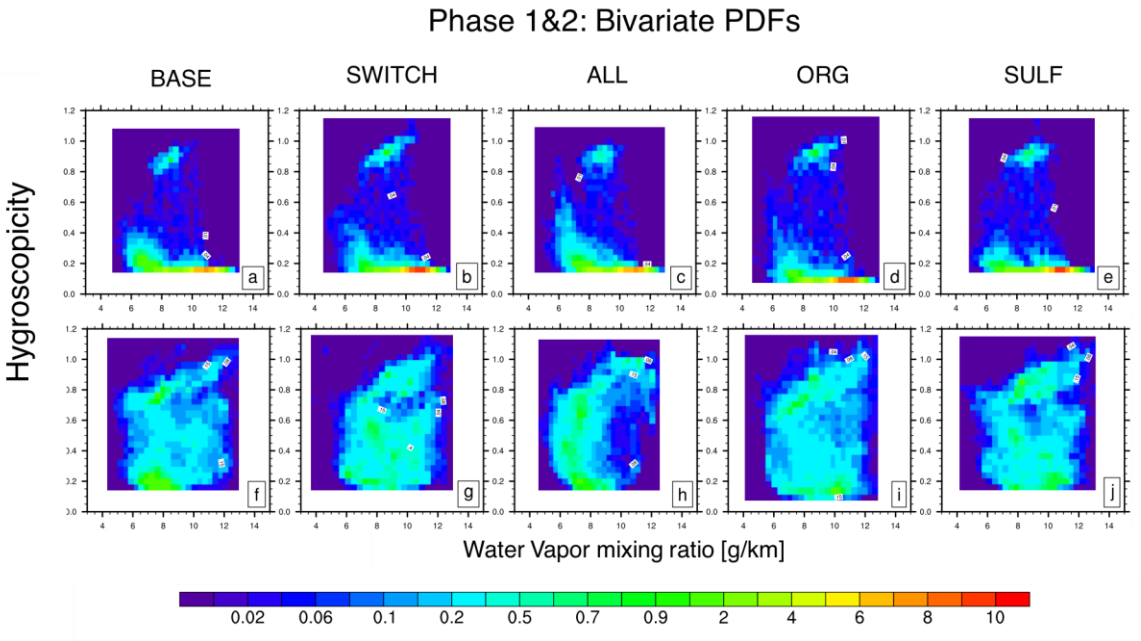

Figure 8: Bivariate probability density function of hygroscopicity and water vapor mixing ratio in g kg^{-1} for phase 1 (a-e), and phase 2 (f-j) for each simulation.

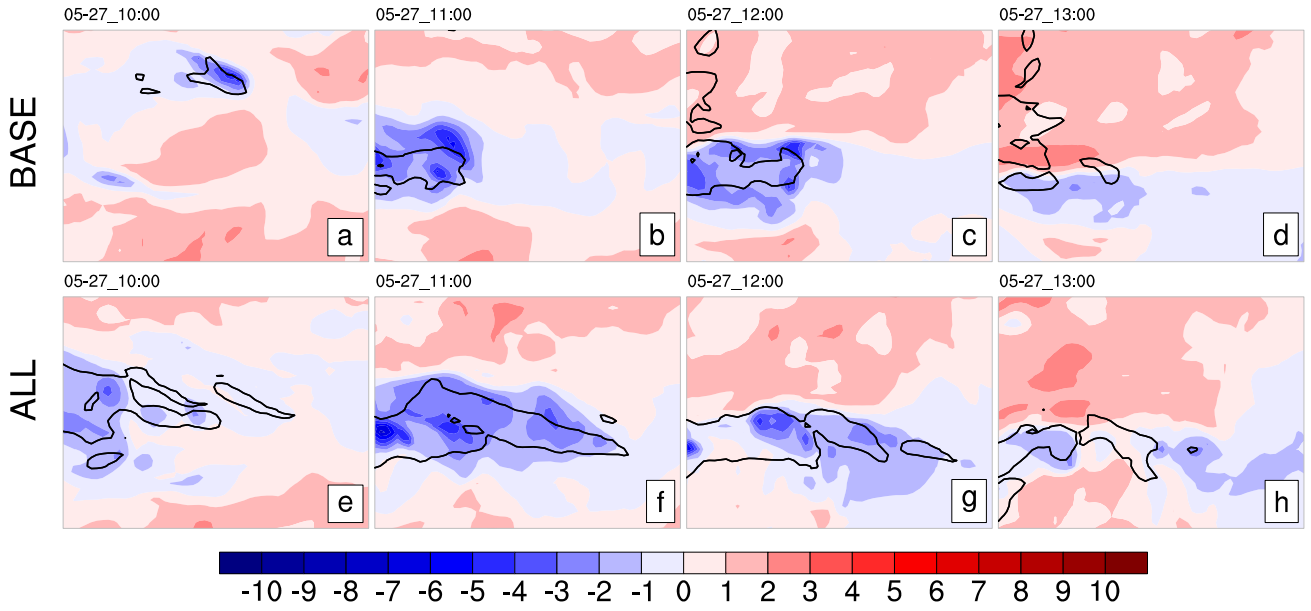

1121

1122 ***Figure 9:*** 10- meter maximum wind speed (12 m s^{-1} contour; solid black line) and the

1123 lowest level perturbation potential temperature (K; blue (negative) and red (positive)

1124 contours) for BASE simulation (a-d) and the ALL simulation (e-f). The black dots

1125 indicate the location of Kansas City, MO.

1126

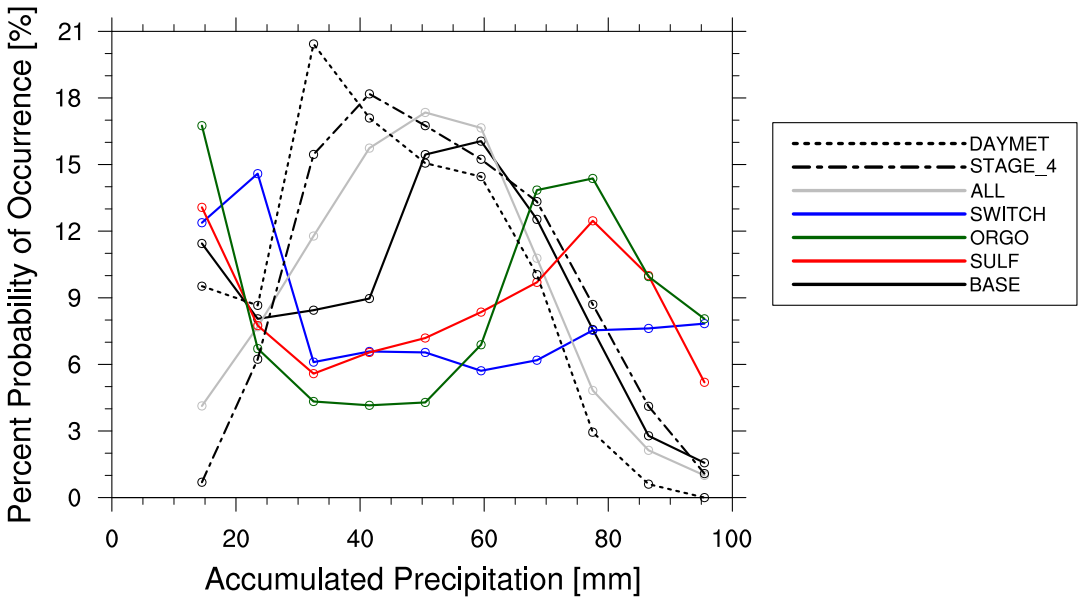

1127

1128 ***Figure 10:*** Probability density function (PDF) of observed (grey) and modeled (BASE-

1129 black, SULF-red, ORG-green, SWITCH-blue, ALL – black dashed) 24-hour accumulated

1130 precipitation calculated over the red box denoted in Figure 2a.

1131
1132
1133
1134
1135

Figure 1.

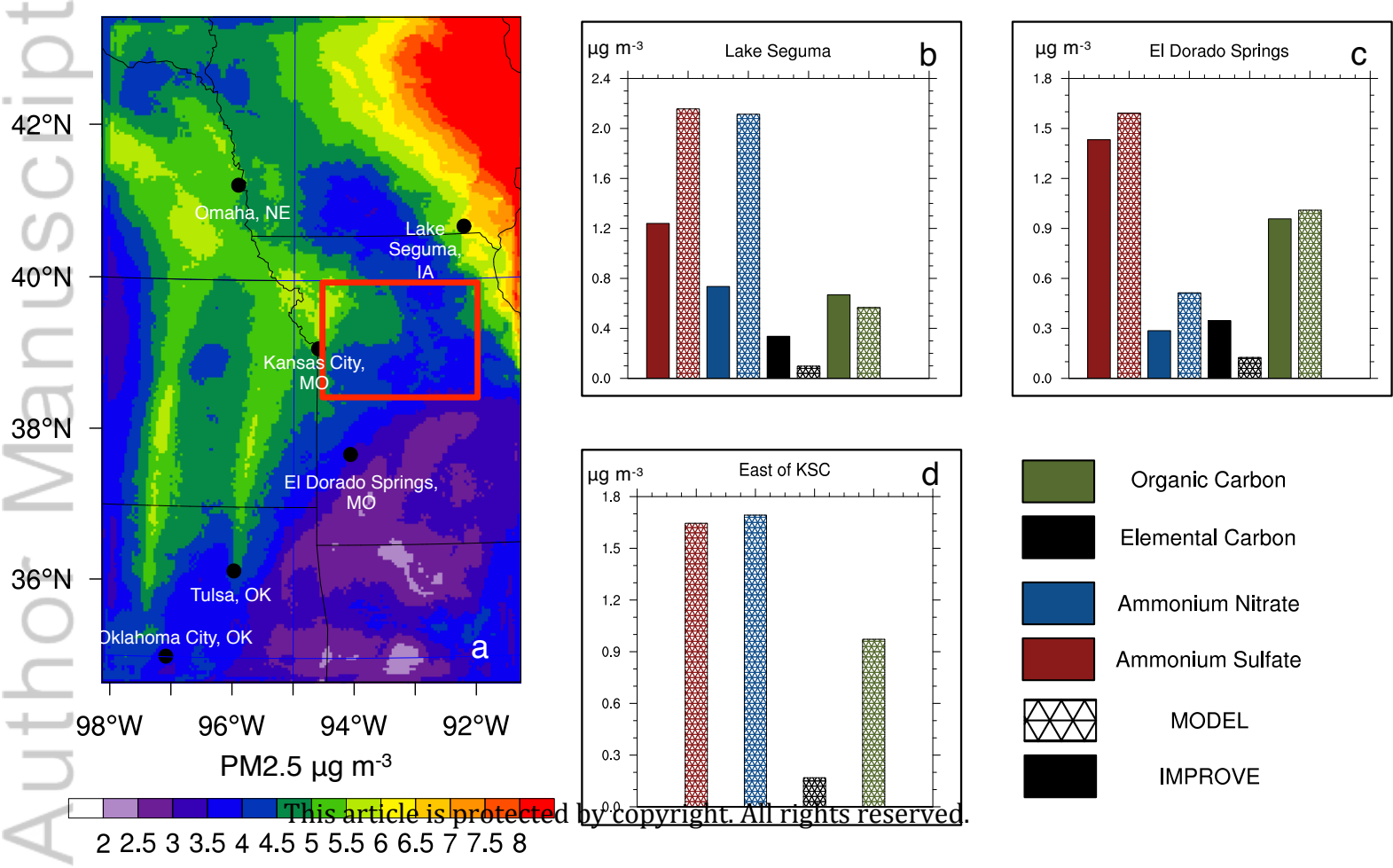

Figure 2.

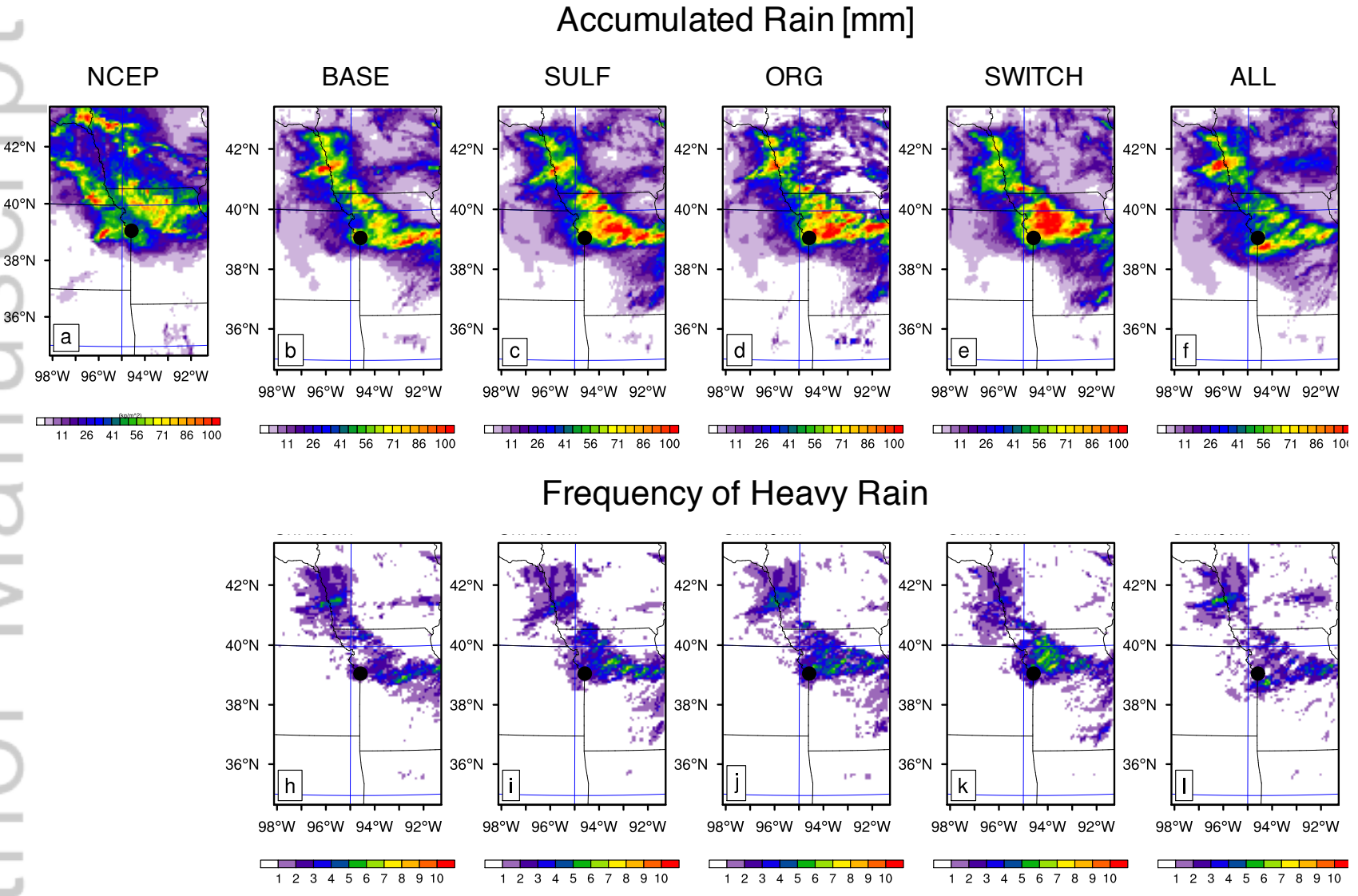

Figure 3.

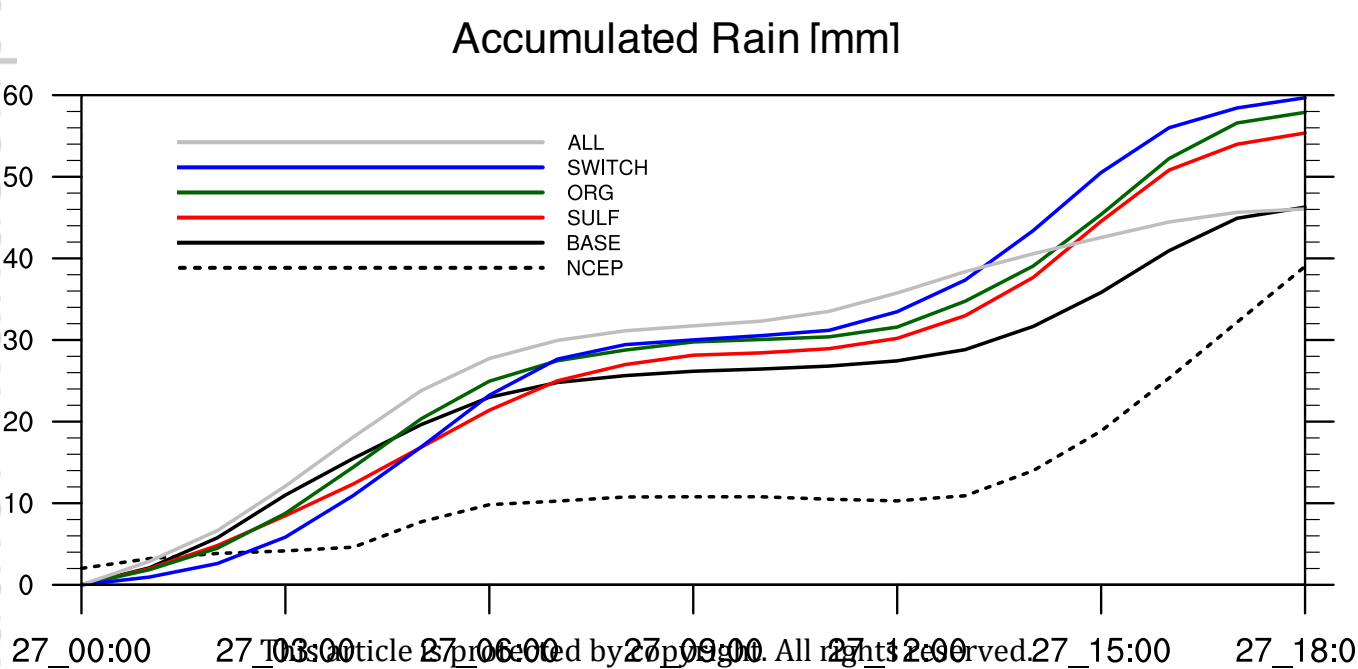

Figure 4.

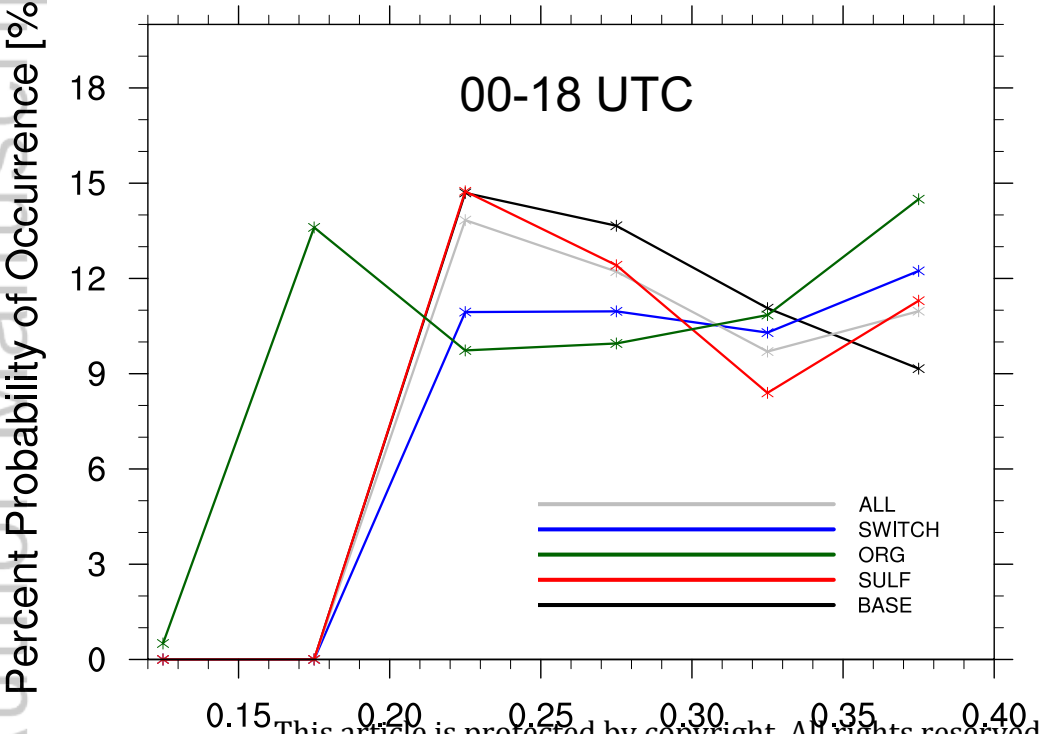

Figure 5.

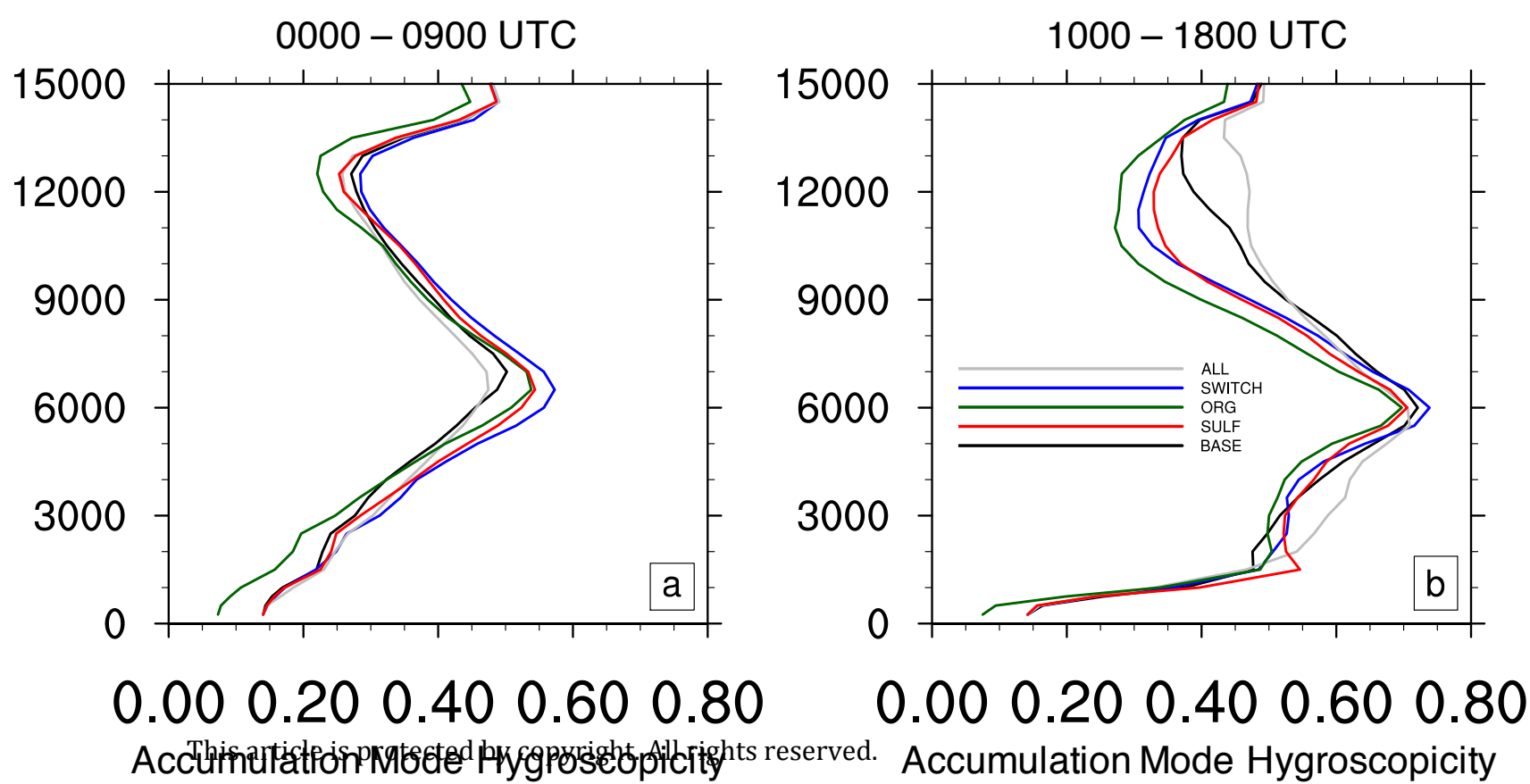

Figure 6.

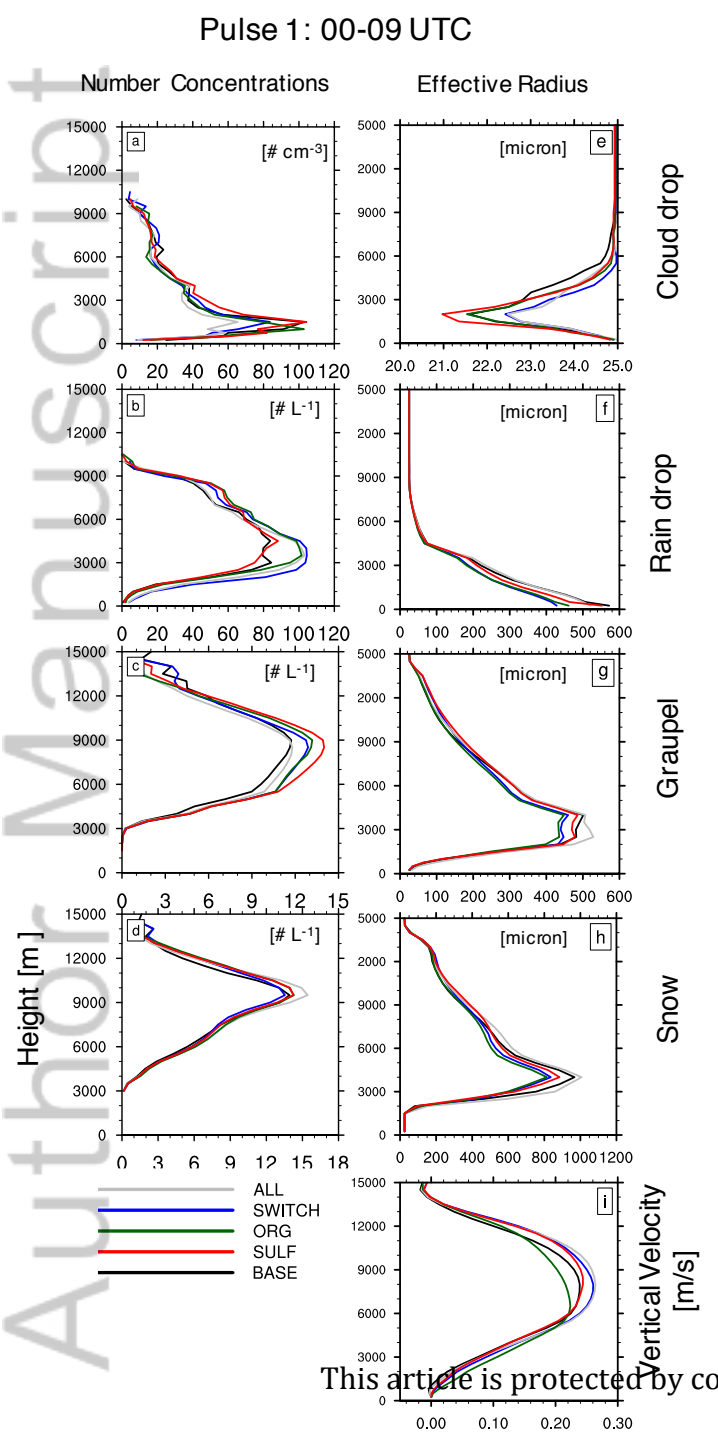

Figure 7.

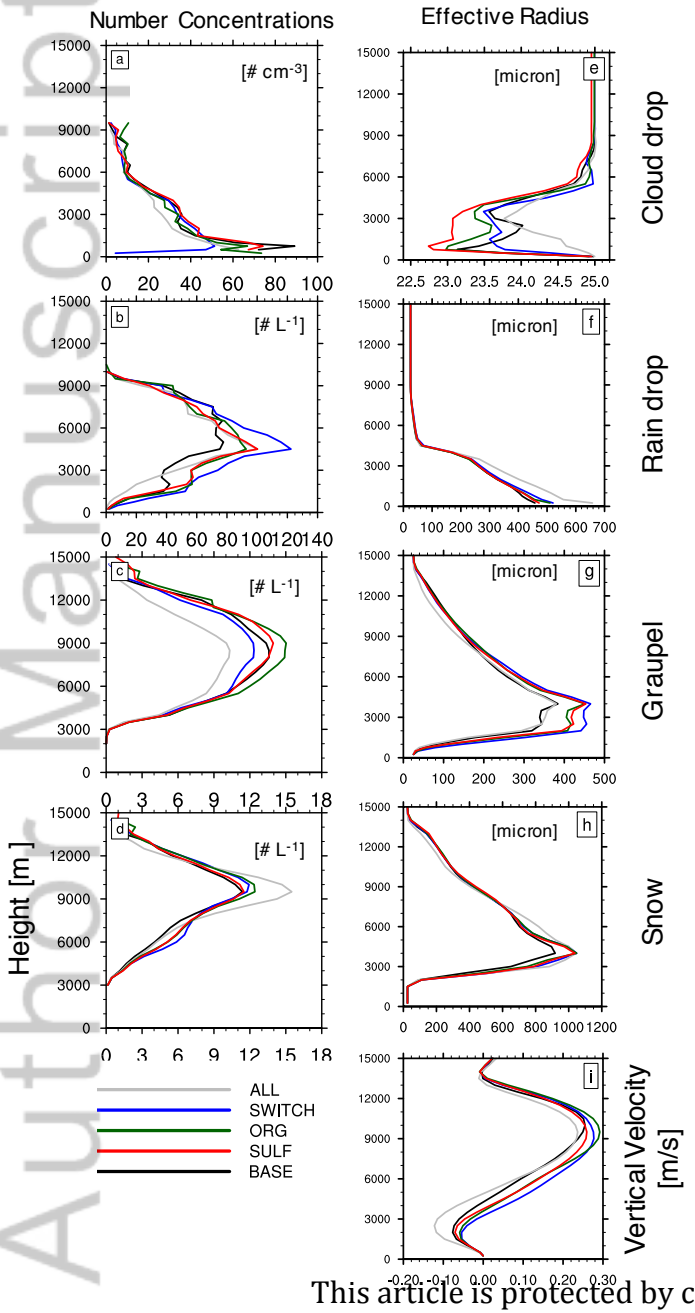

Figure 8.

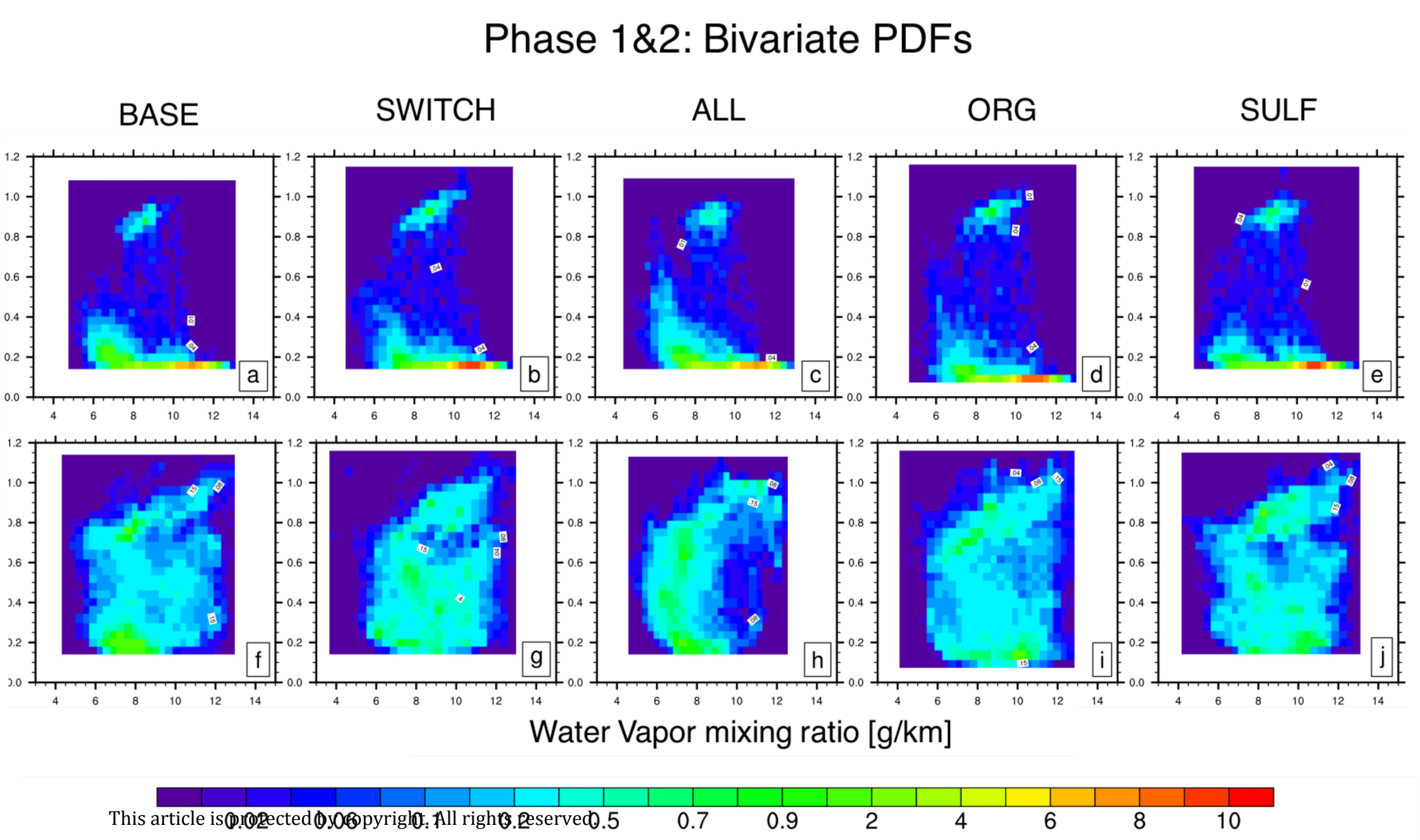

Figure 9.

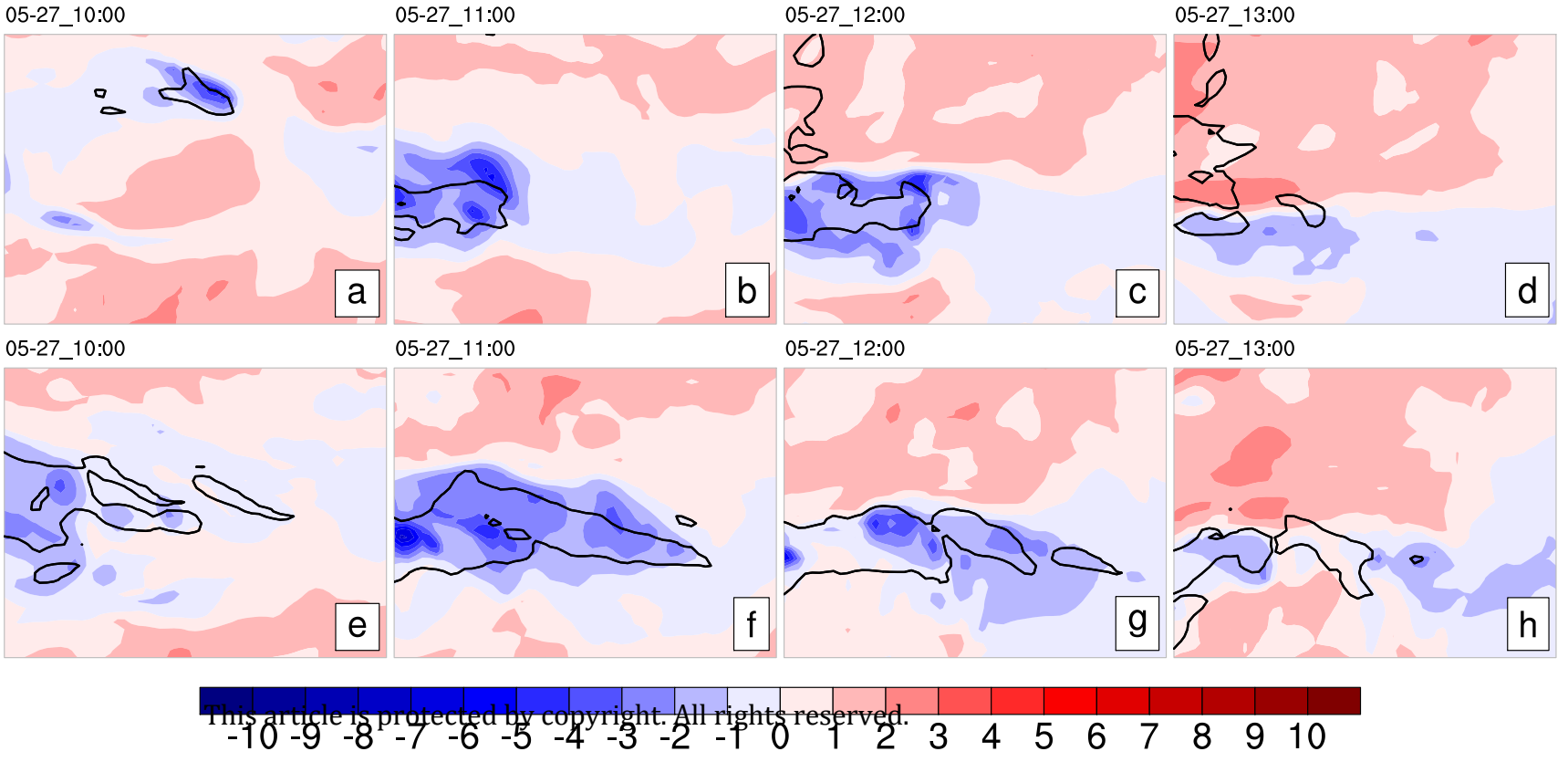

Figure 10.